Synthesizing ultrafast optical pulses with arbitrary spatiotemporal control

Lu Chen[1,2*], Wenqi Zhu[1,2], Pengcheng Huo[3], Junyeob Song[1], Henri J. Lezec[1], Ting Xu[3] and Amit Agrawal[1*]

[1]National Institute of Standards and Technology, Gaithersburg, MD 20899, USA

[2]University of Maryland, College Park, MD 20742, USA

[3]College of Engineering and Applied Physics, Nanjing University, Nanjing 210093, China

*Corresponding authors. e-mail: lu.chen@nist.gov, amit.agrawal@nist.gov

One Sentence Summary: Arbitrary space-time wave packets over an ultrawide bandwidth are synthesized using metasurface optics.

Abstract

The ability to control the instantaneous state of light, from high-energy pulses down to the single-photon level, is an indispensable requirement in photonics. This has, for example, facilitated spatiotemporal probing and coherent control of ultrafast light-matter interactions, and enabled capabilities such as generation of exotic states of light with complexity, or at wavelengths, that are not easily accessible. Here, by leveraging the multifunctional control of light at the nanoscale offered by metasurfaces embedded in a Fourier-transform setup, we present a versatile approach to synthesize ultrafast optical transients with arbitrary control over its complete spatiotemporal evolution. Our approach, supporting an ultrawide bandwidth with simultaneously high spectral and spatial resolution, enables ready synthesis of complex states of structured space-time wave packets. We expect our results to offer new capabilities in coherent ultrafast light-matter interactions, and facilitate applications in microscopy, communications, and nonlinear optics.

INTRODUCTION

From revealing molecular dynamics in the attosecond timescale to generation of high-energy pulses in the petawatt regime, ultrafast optics continues to have far-reaching impacts across a wide range of scientific disciplines (*1-5*). In the time-domain, the high peak intensity associated with an ultrafast pulse has enabled numerous advances in nonlinear optics (*6*) and high-field physics (*7*); whereas, in the frequency-domain, the corresponding equally spaced spectral lines, referred to as frequency combs, have become indispensable for precision metrology and spectroscopy (*8-10*). Generation of ultrafast optical pulses and their use in these various application areas rely in some form on coherently controlling their temporal evolution using techniques commonly referred to as ultrafast optical pulse shaping (*11, 12*). For example, functions such as pulse compression or optical arbitrary waveform generation require temporal control achieved via manipulating the spectral phase and amplitude (*13*, *14*), whereas realization of space-time wave packets requires additional control over the spatial degree of freedom (*15*). Here, using metasurface optics, we present a universal approach towards arbitrary controlling the full space-time evolution of ultrafast optical pulses. We demonstrate the versatility of this approach by generating spatiotemporal waveforms carrying, simultaneously, a rich-set of instantaneous polarization states and time-multiplexed spatial wavefronts with different topological charges. This is made possible by the use of metasurfaces which offer multidimensional control of light at the nanoscale (*16*), enabling simultaneous and independent control of the phase, amplitude, polarization and spatial wavefront of spectrally dispersed ultrafast pulses. The nanoscale control further breaks the constraint in both spectral and spatial resolution placed by the large pixel size of traditional pulse modulation techniques, enabling synthesis of arbitrary space-time wave packets over an ultrawide bandwidth. We expect our results to enable novel capabilities in probing and manipulation of ultrafast

molecular (*17, 18*) or topological (*19, 20*) excitations, or in generation of complex states of extreme-ultraviolet (EUV) (*21, 22*) or x-ray light (*23, 24*).

RESULTS

We describe our approach of synthesizing arbitrary spatiotemporal pulses by treating an ultrafast pulse train as a frequency comb, where the pulse train spectrum is composed of a series of equally spaced spectral lines at frequencies given by $\nu_j = j\nu_{\mathrm{rep}} + \nu_0$, where j is an integer, ν_{rep} is the repetition rate of the laser and ν_0 is the carrier-envelope offset frequency (*9*). Assuming an input beam of Gaussian spatial and spectral distribution, the transform-limited spatiotemporal electric field $\vec{\boldsymbol{E}}_{\mathrm{in}}$ (here the arrow accent denotes the vectorial nature of the field whereas the bold font denotes that the field is complex) of a *p*-polarized (*E*-field parallel to the *x*-axis) input pulse train can be expressed by its Fourier series:

$$\vec{\boldsymbol{E}}_{\mathrm{in}}(x,y,t) = \sum_j e^{-\frac{x^2}{\sigma^2}} e^{-\frac{y^2}{\sigma^2}} \cdot a_j e^{-i\omega_j t} \begin{bmatrix} 1 \\ 0 \end{bmatrix}, \tag{1}$$

where σ represents the input beam waist, a_j is the spectral amplitude and $\omega_j = 2\pi\nu_j$. At the input of a Fourier transform (FT) pulse shaper (Fig. 1A), the various spectral lines constituting the ultrafast pulse train are first angularly dispersed by a blazed grating and focused at the Fourier plane (ξ, η) using an off-axis parabolic mirror, transforming the input electric field into $\vec{\boldsymbol{E}}_{-}(\xi,\eta,t) \propto \mathcal{F}\left\{\mathcal{G}\{\vec{\boldsymbol{E}}_{\mathrm{in}}(x,y,t)\}\right\} = \sum_j u_j(\xi - \xi_j) u_j(\eta) a_j e^{-i\omega_j t} \begin{bmatrix} 1 \\ 0 \end{bmatrix}$, where $\vec{\boldsymbol{E}}_{-}$ is the electric field at the input of the metasurface at the Fourier plane with the individual spectral lines ω_j dispersed along the ξ-axis, $\mathcal{F}$ is the Fourier transform, $\mathcal{G}$ represents the grating function, and $u_j(\xi)$ is the one-dimensional (1D) spatial Fourier transform of the input field at ω_j (see Supplementary Text S1). A transmission-mode dielectric metasurface placed at the Fourier plane is designed to

impart a complex masking Jones matrix $\boldsymbol{M}(\xi,\eta)$ to the spectrally dispersed electric-field $\vec{\boldsymbol{E}}_-$, resulting in an electric field $\vec{\boldsymbol{E}}_+(\xi,\eta,t) = \begin{bmatrix} \boldsymbol{M}_p \boldsymbol{E}_-(\xi,\eta,t) \\ \boldsymbol{M}_s \boldsymbol{E}_-(\xi,\eta,t) \end{bmatrix}$ at the exit plane of the metasurface. Here, $\boldsymbol{M}_p$ and $\boldsymbol{M}_s$ are the corresponding $\boldsymbol{M}(\xi,\eta)$ elements that respectively determine the *p*- and *s*- polarized components of $\vec{\boldsymbol{E}}_+$ for an input *p*-polarized electric-field $\vec{\boldsymbol{E}}_-$. This combination of Fourier decomposition coupled with the multidimensional control at the nanoscale offered by metasurfaces, enables us to parallelly and independently manipulate the full spatial and temporal properties of each spectral component.

To achieve this, we spatially divide the metasurface into Q superpixels S_J (J = 1, 2, … Q) linearly concatenated along the ξ-axis, where each superpixel S_J acts as a sub-metasurface of its own offering a polarization-multiplexed spectral modulation $\boldsymbol{\Upsilon}_J^{p(s)}(\omega_J)$, and spatial modulation $\boldsymbol{\Gamma}_J^{p(s)}(\xi-\xi_J,\eta)$, targeted to tailor the complex transmission of a small spectral subrange $\Delta\lambda_J$, centered at λ_J. The complex masking function $\boldsymbol{M}_{p(s)}$ of the entire metasurface can therefore be expressed in terms of an assembly of complex masking functions of individual superpixels as,

$$\boldsymbol{M}_{p(s)}(\xi,\eta) = \sum_{J=1}^{Q} \boldsymbol{\Upsilon}_J^{p(s)}(\omega_J)\boldsymbol{\Gamma}_J^{p(s)}(\xi-\xi_J,\eta)\Pi(\xi-\xi_J), \tag{2}$$

where $\Pi(\xi-\xi_J)$ represents a rectangular function that defines the boundary of superpixel S_J. Each superpixel is further divided into a two-dimensional (2D) array of square pixels of pitch p_J, each consisting of a subwavelength-size dielectric nanopillar of rectangular cross-section acting as a birefringent waveplate (Fig. 1A, insets). To achieve the multifunctionality required at the nanoscale, a library of birefringent nanopillars at each ω_J is generated to simultaneously provide $\Phi_1(\xi,\eta)$ and $\Phi_2(\xi,\eta)$ covering the full [0, 2π] range, where Φ_1 and Φ_2 are the respective phase

shifts along the two birefringent axes of the nanopillar. Therefore, via a judicious choice of nanopillars constituting each superpixel with spatially varying in-plane dimensions (L_1 and L_2) and rotation angles (θ), independent control of spatial wavefront, phase, amplitude, and polarization for each spectral subrange $\Delta\lambda_J$ can be achieved. Finally, the modulated spectral components at the output of the metasurface are recombined using a second pair of parabolic mirror and grating, resulting in a synthesized output pulse train with an electric field $\vec{\boldsymbol{E}}_{\mathrm{out}}$ given by:

$$\vec{\boldsymbol{E}}_{\mathrm{out}}(x,y,t) = \begin{bmatrix} \sum_{J=1}^{Q} \boldsymbol{E}^{p}_{\mathrm{out},J}(t)\boldsymbol{E}^{p}_{\mathrm{out},J}(x,y) \\ \sum_{J=1}^{Q} \boldsymbol{E}^{s}_{\mathrm{out},J}(t)\boldsymbol{E}^{s}_{\mathrm{out},J}(x,y) \end{bmatrix}, \tag{3}$$

where $\boldsymbol{E}^{p(s)}_{\mathrm{out},J}(t) = a_J \boldsymbol{\Upsilon}^{p(s)}_J(\omega_J) e^{-i\omega_J t}$ and $\boldsymbol{E}^{p(s)}_{\mathrm{out},J}(x,y) = \mathcal{F}^{-1}\left\{\boldsymbol{\Gamma}^{p(s)}_J(\xi,\eta)\Pi(\xi)u_J(\eta)\right\}$ represent the independent spectral and spatial shaping of the *p*- (*s*-) polarized spectral components centered at ω_J, respectively (see Supplementary Text S1). The novelty of the approach outlined above stems from the fact that it provides parallel control over the temporal state of light via engineering the metasurface at the superpixel level while enabling simultaneous control over its spatial wavefront evolution via engineering individual nanopillars within each superpixel (Fig. 1B).

Experimentally, pulse synthesis is achieved by placing the metasurface at the Fourier plane (ξ,η) of a custom-built FT pulse shaper (see Materials and Methods). The metasurface is designed to address spectrally dispersed linearly-polarized input pulses from a Ti:sapphire oscillator (pulse duration <10 fs, corresponding to a full-width at tenth-maximum bandwidth of ≈80 THz at a central wavelength of $\lambda_c = 800$ nm). We divide the metasurface into Q = 201 superpixels, each of size 115 μm × 200 μm, to match the optimized spectral resolution $\Delta\lambda_J$ = 1 nm of the implemented pulse

synthesizer. To demonstrate our ability of simultaneous spatiotemporal control, as an illustrative example, we first design a metasurface optic to transform an input *p*-polarized, Gaussian wavefront ultrafast pulse to a shaped pulse exhibiting, simultaneously, a time-varying polarization state, and a vortex spatial wavefront carrying an orbital angular momentum (OAM) order of $\ell = -1$ (Fig. 2, A and B). The control of instantaneous polarization requires each superpixel S_J to simultaneously endow complex spectral masking functions $\boldsymbol{\Upsilon}_J^p(\omega_J) = \cos\left(b_{\mathrm{I}}(\omega_J - \omega_{\mathrm{c}})\right) e^{i\frac{b_{\mathrm{II}}}{2}(\omega_J - \omega_{\mathrm{c}})^2}$ and $\boldsymbol{\Upsilon}_J^s(\omega_J) = i\sin\left(b_{\mathrm{I}}(\omega_J - \omega_{\mathrm{c}})\right) e^{i\frac{b_{\mathrm{II}}}{2}(\omega_J - \omega_{\mathrm{c}})^2}$ to the spectrally dispersed electric-field components $\vec{\boldsymbol{E}}_{-,J}$, where b_{I} and b_{II} are the group delay and group delay dispersion, respectively, and ω_{c} is the angular frequency at λ_{c}. Concurrently, the spatial wavefront control is achieved by imparting a spiral-phase transformation $\boldsymbol{\Gamma}_J^{p(s)}(\xi - \xi_J, \eta) = e^{i\ell_J \tan^{-1}\frac{\eta}{\xi - \xi_J}}$ to each superpixel S_J, where $\ell_J = -1$. These simultaneous requirements define the targeted masking functions $\boldsymbol{M}_p(\xi, \eta)$ and $\boldsymbol{M}_s(\xi, \eta)$, which can be satisfied by leveraging the library of birefringent nanopillars and placing each nanopillar at $\theta = \pi/4$. The implemented phase topography is given by $\Phi_{1(2)}(\omega_J, \xi, \eta) = \varphi_{1(2)}(\omega_J) - \tan^{-1}\frac{\eta}{\xi - \xi_J}$ for each superpixel S_J (see Supplementary Text S2), where $\varphi_{1(2)}(\omega_J) = \frac{b_{\mathrm{II}}}{2}(\omega_J - \omega_{\mathrm{c}})^2 \pm b_{\mathrm{I}}(\omega_J - \omega_{\mathrm{c}})$ represents the corresponding spectral phase, b_{II} governs the temporal length of the synthesized pulse, and $b_{\mathrm{I}}/b_{\mathrm{II}}$ determines the rotation-speed of the major-axis of instantaneous polarization (see Supplementary Text S3). For the experiment, by setting $b_{\mathrm{II}} = 100$ fs^2/rad and $b_{\mathrm{I}}/b_{\mathrm{II}} = 0.1$ rad/fs, the corresponding $\varphi_{1(2)}$ *vs.* λ, and $\Phi_{1(2)}$ for eight representative superpixels ($J = 34$ to 41, corresponding to $\lambda_J = 733$ nm to 740 nm) are plotted in Fig. 2 (C and D), respectively. Each nanopillar in-plane dimension $L_{1(2)}(\omega_J, \xi, \eta)$ that simultaneously satisfies the local phase requirements for each ω_J and offers the highest

transmission is determined via minimization of a figure-of-merit (*FOM*) function (see Materials and Methods). One representative plot illustrating the dependence of *FOM vs.* (L_1, L_2) to simultaneously endow $\Phi_1 = 0.90\pi$ and $\Phi_2 = 1.54\pi$ at one nanopillar location within a superpixel at $\lambda_J = 734$ nm (white cross, Fig. 2D), is shown in Fig. 2E (*FOM* minima denoted by the white circle). The *FOM* minimization procedure, repeated at each λ_J, yields a library of $L_{1(2)}$ values that simultaneously satisfies any requisite $\Phi_{1(2)}$ combination covering the full [0, 2π] range (see fig. S4 for one representative library at $\lambda_J = 734$ nm). The requisite nanopillars constituting the metasurface are patterned on a layer of 650 nm thick amorphous-Si (a-Si) on fused-silica substrate using electron-beam lithography and reactive ion etching (see Materials and Methods). An optical transmission image of the fabricated metasurface, of dimension 2.3 cm × 200 μm, taken under unpolarized white-light illumination along with a higher-magnification image of eight superpixels (corresponding to $J = 34$ to 41, Fig. 2D) and a representative scanning electron microscope (SEM) image are shown in Fig. 2 (F and G), respectively.

The complete spatiotemporal evolution of the synthesized OAM-carrying, polarization-swept pulse, $\vec{\boldsymbol{E}}_{\text{out}}(x, y, t)$, at the output of the pulse shaper is characterized by using a combination of spectral and spatial domain methods (Fig. 3). Measuring the temporal polarization evolution of the pulse requires measurement of the spectral intensity $(I_{p(s)}(\omega_J))$ and phase $(\varphi_{p(s)}(\omega_J))$ for the two orthogonal *p*- and *s*- polarized components. $I_{p(s)}(\omega_J)$ is measured by directing the *p*- (*s*-) polarized component of $\vec{\boldsymbol{E}}_{\text{out}}$ to a grating spectrometer, whereas $\varphi_{p(s)}(\omega_J)$ is measured using a custom-built spectral interferometry setup. Spectral interferometry is performed by interfering the synthesized pulse $\vec{\boldsymbol{E}}_{\text{out}}$ with a transform-limited reference pulse $\vec{\boldsymbol{E}}_{\text{in}}$ that was partially split at the input of the pulse shaper, at a fixed time-delay $\tau = \tau_0$ (see Materials and Methods). The temporally evolving polarization state of the experimentally measured pulse is characterized by

measuring the temporal amplitude $A_{p(s)}(\tau)$ of the *p*- (*s*-) polarized component and the phase difference $\Psi_p(\tau) - \Psi_s(\tau)$, which closely matches the design (Fig. 4A). The Poincaré sphere representation of the measured temporal polarization state (Fig. 4B) also closely resembles the design (Fig. 2B). The time-averaged spatial intensity distribution of the two polarization components, $\bar{I}_{p(s)}(x, y)$, is measured by imaging the *p*- (*s*-) polarized component of $\vec{\boldsymbol{E}}_{\text{out}}$ on a CMOS sensor (Insets, Fig. 4A); whereas, the vortex spatial phase distribution, $\Psi_{p(s)}(x, y, t)$, for the two polarization components, is confirmed by spatially interfering $\vec{\boldsymbol{E}}_{\text{out}}$ with $\vec{\boldsymbol{E}}_{\text{in}}$ at different time delay τ. Three representative spatial interference images, each for *p*- and *s*- polarized components, taken at $\tau = -27$ fs, 0 fs and $+27$ fs (red, green and blue stars, respectively, Fig. 4B), clearly show a single-fork dislocation confirming that, as designed, the entire synthesized pulse is carrying $\ell_J = -1$. The fine structure in experimentally measured $\bar{I}_{p(s)}(x, y)$ stems from the astigmatism-limited spot size and finite spectral resolution of the implemented FT pulse shaper ($\Delta\lambda_J$ = 1 nm), nominally corresponding to ≈6250 spectral lines each illuminating a superpixel at a slightly shifted spatial location ξ_j. The effect of spatially dispersed illumination within each superpixel S_J, including overlap at boundaries with adjacent superpixels $S_{J\pm1}$, is numerically modelled by calculating $\boldsymbol{E}_{+,J}(\xi, \eta, t)$ accounting for all spectral lines illuminating each S_J, and propagating it through the pulse shaper yielding a far-field response $\boldsymbol{E}_{\text{out},J}(\xi, \eta, t)$ (see Supplementary Text S4). The simulated far-field intensity resulting from one representative superpixel (S_{101}), $\bar{I}_{\text{out},101}(x, y)$, accounting for all 6250 spectral lines illuminating it, shows a perturbed doughnut-shape resulting from the non-uniform superpixel illumination (Fig. 4C, left). The corresponding calculated far-field phase distribution, $\Psi_{\text{out},101}(x, y, t = 0)$, shows a perturbed 2π phase winding, confirming the synthesis of a vortex wavefront carrying $\ell_J = -1$ (Fig. 4C,

right). The numerically calculated $\bar{I}_{\mathrm{out}}(x,y) = \sum_J \bar{I}_{\mathrm{out},J}(x,y)$, representing the collective far-field response from the entire metasurface and accounting for all 201 superpixels (Fig. 4D), closely resembles the experimentally measured intensity distribution (Fig. 4A, insets). The full analytical formulation and numerical results describing the synthesis of spatiotemporal wave packets are presented in Supplementary Text S1 and S4.

The high spatial and spectral resolution, full-design freedom, and ready-extension to other spectral ranges either linearly or nonlinearly, make our approach an attractive platform for simple realization of other form of space-time wave packets over an ultrawide bandwidth. For example, these capabilities immediately lend themselves for generation of complex light states such as those exhibiting dynamic rotation and revolution (*25*) or possessing time-varying OAM (*22*), which either have only been proposed theoretically or are limited to the EUV regime via high-harmonic generation. To illustrate this, we synthesize two analogs of space-time wave packets: a light-coil representing a transform-limited pulse with helical intensity distribution (*26*); and another, exhibiting coherently multiplexed time-varying OAM orders. These requisite functionalities are achieved by imparting a prescribed ℓ_J to a preassigned set of ω_J constituting the pulse, while simultaneously controlling their spectral phase $\varphi_{1(2)}(\omega_J)$. We experimentally demonstrate this by fabricating a metasurface able to encode five time-multiplexed topological charges to an ultrafast pulse, and controlling its group delay dispersion b_{II}, implemented via superpixel masking function, $\boldsymbol{M}_J = e^{i\frac{b_{\mathrm{II}}}{2}(\omega_J-\omega_{\mathrm{c}})^2} e^{i\ell_J \tan^{-1}\frac{\eta}{\xi-\xi_J}} \Pi(\xi-\xi_J)$, where $\ell_J = +2, +1, 0, -1$ or -2 is assigned to each S_J within five prescribed spectral sub-regions (Fig. 5A). An optical transmission image of the fabricated metasurface along with a higher-magnification image of five representative superpixels ($J = 26, 56, 101, 146$ and 171), their intensity transmission $I_{+,J}$ measured using a tunable

continuous wave (cw-) laser at the corresponding λ_J, and the spatial interferogram I_J^{intf} measured via interference of $\boldsymbol{E}_{+,J}$ with a reference Gaussian beam of the same color confirm that, as designed, each S_J is able to impart the desired ℓ_J to each ω_J (Fig. 5A). The corresponding mode purity of the OAM beams is calculated to be 0.68, 0.80, 0.75, 0.69, 0.58, respectively, using the method outlined in ref. *27*. When transform limited ($b_{\mathrm{II}} = 0$ fs^2/rad), coherent interference of the various ℓ_J orders at each time-instance t results in a radially displaced, spatiotemporally localized wave packet that revolves azimuthally around a central propagation axis (Fig. 5B). Subsequently, introduction of a chirp ($b_{\mathrm{II}} = 180$ fs^2/rad) to the masking function $\boldsymbol{M}_J$, results in temporal separation of the various ω_J, or equivalently ℓ_J, where the pulse now exhibits a time-varying vortex spatial phase topography. In each case, the spatiotemporal evolution of the generated pulse is determined from the measured interferograms $I_{\mathrm{intf}}(x, y, \tau)$, resulting from the interference of $\boldsymbol{E}_{\mathrm{out}}(x, y, t)$ with a reference pulse $\boldsymbol{E}_{\mathrm{in}}$ at different time delay τ. The reconstructed spatiotemporal wave packet $I_{\mathrm{meas}}(x, y, \tau)$ of the synthesized light-coil, exhibiting a localized intensity revolving around a central propagation axis, closely matches the numerically simulated intensity distribution, $I_{\mathrm{sim}}(x, y, t)$ (Fig. 5B). For the synthesized time-varying OAM pulse, three-representative $I_{\mathrm{intf}}(x, y)$ snapshots clearly show three distinct OAM states at different τ, closely matching the numerically simulated spatiotemporal phase evolution, $\Psi_{\mathrm{sim}}(x, y, t)$ (Fig. 5C). The retrieved mode-purity for the simulated pulse along with those of the three experimental snapshots in Fig. 5C are shown in fig. S11. The complete spatiotemporal evolution of $I_{\mathrm{sim}}(x, y, t)$ and $\Psi_{\mathrm{sim}}(x, y, t)$ along with the corresponding $I_{\mathrm{meas}}(x, y)$ and $I_{\mathrm{intf}}(x, y)$ *vs*. τ for the two synthesized pulses are analytically modelled and experimentally captured (see Supplementary Text S5 and Supplementary Movies S1 and S2), illustrating the rich diversity and control over the spatiotemporal encoding of a single ultrafast pulse.

DISCUSSION

In summary, by leveraging the multidimensional control of light at the nanoscale offered by metasurfaces, we have experimentally demonstrated a versatile photonic platform able to control the complete four-dimensional spatiotemporal evolution of ultrafast pulses over an ultrawide bandwidth. Beyond the exquisite time-varying polarization and temporally encoded spatial-wavefront evolution demonstrated here, our approach can be simply extended to other forms of structured light (*28*) or space-time wave packets (*29, 30*) via superpixel engineering, or wavelength regimes via nonlinear control (*31*). While the functionalities achieved in this work are static, we expect ongoing research in the field of active metasurfaces to in-time provide capabilities required for reconfigurable control (*32*).

MATERIALS AND METHODS

Spatiotemporal pulse shaping setup

Input femtosecond pulses, of duration ≈ 10 fs and time-averaged power ≈ 400 mW, centered at 800 nm (full-width at tenth-maximum bandwidth of ≈ 80 THz), are generated at a repetition rate of 75 MHz from a Ti:sapphire oscillator. An ultrafast beam splitter is used to transmit 75 % of the input power into the pulse shaper and reflect the remaining 25 % into the reference beam (Fig. 3). At the input of the pulse shaper, the beam has a Gaussian spatial profile of diameter ≈1 cm ($1/e^2$ of the maximum intensity). The frequency components constituting the pulse are first angularly dispersed by a blazed grating (300 grooves per millimeter) into the first diffraction order, and then focused by an off-axis metallic parabolic mirror (reflected focal length $f = 381$ mm and an off-axis angle of 15°). The diffraction efficiency of the gratings differs by ≲10 % between the *p*- and *s*- polarization over the spectral range from 700 nm to 900 nm. The grating-mirror pair is used to spatially disperse the input beam over the full length of the metasurface along the ξ-direction, following a quasi-linear function $\lambda(\xi)$ (fig. S1). Using ray tracing simulations, an effective monochromatic spot size at the center wavelength of $\lambda_c = 800$ nm is estimated to be ≈34 μm, corresponding to a theoretical upper limit on the wavelength resolution of ≈0.3 nm or a spectral resolution of $\Delta\omega_j = 140$ GHz for the implemented Fourier-transform (FT) pulse shaper (*33*). In the experiments, metasurfaces consisting of $Q = 201$ superpixels, each of size 115 μm × 200 μm, correspond to an implemented $\Delta\omega_J \approx 467$ GHz at λ_c, wherein the spectral resolution is sacrificed to minimize boundary effects between adjacent superpixels (see Supplementary Text S4). Along the η-direction, the largest astigmatism-limited spot at the edge of the spectrum is ≈ 0.2 mm.

The alignment of the metasurface at Fourier-plane involves translation along ξ-, η-, and z-directions, roll within the (ξ, η) plane, pitch within the (η, z) plane, and yaw within the (ξ, z) plane. A linear translation stage is used to control the z-direction translation, and a six-axis kinematic mount is further used to control the ξ- and η- translation, the pitch and yaw adjustment and roll-rotation. Nine reference half-waveplate metasurface superpixels are fabricated parallel to the pulse-shaping metasurfaces to facilitate alignment along the ξ-direction. By monitoring the spectrum of the transmitted light through the reference metasurface superpixels (fig. S1), rigorous alignment of the ξ-position is achieved. Yaw and pitch are aligned using the back reflection from the metasurface. Note that the metasurface is intentionally placed at a small pitch angle (≈ 2º) to minimize any back reflection into the laser system. The remaining η- and roll- alignments are performed by sequentially allowing either the long or the short end of the spectrum to transmit while blocking the remaining frequencies at the Fourier plane, and monitoring the intensity in the far-field.

Assuming the input pulse follows a Gaussian intensity distribution with peak power at $\lambda_c = 800$ nm and accounting for diffraction loss from the grating, the peak intensity incident on the nanopillars ≤ 300 kW/cm^2, where we do not expect any significant nonlinear effects inside the a-Si nanopillars (*34*). After passing through the metasurface, the beam is recombined using a second parabolic mirror and grating pair, yielding a vectorially shaped pulse of desired spatiotemporal characteristics. The complete time-varying properties of the recombined pulse exiting the system are measured using a combination of spatial and spectral domain techniques described below.

Metasurface simulation and design

The transmission amplitudes t_1, t_2 and phase shifts ψ_1, ψ_2 along the two birefringent axes of a rectangular nanopillar are simulated for wavelengths $\lambda_J = (699 + J)$ nm, where $J = 1,2, \ldots, 201$

using rigorous coupled wave analysis (*35*), for all combinations of lateral nanopillar sizes $L_1, L_2 \in [0.15p, 0.86p]$, where $p(\lambda) = (0.4\lambda - 60\ \text{nm})$ is the pitch of the unit-cell along both the ξ and η directions. The wavelength-dependent complex refractive indices for amorphous silicon (a-Si) used in the simulations is measured using spectroscopic ellipsometry (fig. S2). We also performed Raman spectroscopy on the electron-beam exposed a-Si to ensure no morphological change occurred during exposure (fig. S3). For a given position (ξ, η) in the Fourier plane, the desired spatiotemporal shaping function $\boldsymbol{M}(\xi, \eta)$ (see Supplementary Text S1) is projected onto the two birefringent axes of the nanopillar to impart respectively the targeted complex transmission $e^{i\Phi_1}$ and $e^{i\Phi_2}$. Further, we define the figure-of-merit function (*FOM*) as:

$$FOM(L_1, L_2) = \left|e^{i\Phi_1} - t_1 e^{i\psi_1}\right|^2 + \left|e^{i\Phi_2} - t_2 e^{i\psi_2}\right|^2. \quad (4)$$

The nanopillar dimensions $L_1(\xi, \eta)$, $L_2(\xi, \eta)$ for a given height *H* that simultaneously satisfy the criteria of required phase shifts and offer the highest transmission are identified by the local minimum in the *FOM* map (one representative example is shown in Fig. 2E). The *FOM* minimization process yields a library of L_1, L_2 values that provide the full [0, 2π] phase coverage while maintaining high transmission for each ω_J (one representative library at $\lambda_{J=35} = 734$ nm is shown in fig. S4). Using the libraries, any requisite $\Phi_{1(2)}$ can be satisfied. For example, the simulated $\Phi_{1(2)}$ and $t^2_{1(2)}$ map to achieve the design of the eight representative superpixels (Fig. 2D) are shown in fig. S5A-D, and the average transmission $\bar{t}^2_{1(2)}$ for each superpixel S_J of the entire metasurface is shown in fig. S5E.

Metasurface fabrication

A layer of 650 nm thick a-Si is first deposited on a 500 μm thick fused-silica substrate using plasma-enhanced chemical vapor deposition (PECVD). Here, a-Si thickness of 650 nm is chosen to concurrently satisfy the requirements on achieving the desired phase-depth at longer wavelengths and minimizing optical losses at shorter wavelengths. The substrate is then coated with a 300 nm thick layer of electron beam resist and a 15 nm thick aluminum (Al) anti-charging layer for electron-beam lithography (EBL). The nanopillar designs and alignment marker patterns are exposed using a 100 keV EBL system, followed by Al-layer removal with tetramethylammonium hydroxide (TMAH), and resist development at 4 °C. Next, a 50 nm thick Al_2O_3 layer is deposited by electron beam evaporation. The developed pattern in the resist layer is subsequently transferred to the Al_2O_3 layer via lift-off process. The resulting Al_2O_3 pattern is used as a hard mask for etching a-Si nanopillars using inductively-coupled-plasma reactive ion etching (ICP-RIE), with a mixture gas of SF_6 and C_4F_8 (1:2 ratio) at 1800 W ICP power and 15 W radio frequency power, at 15 °C. The metasurface device is finally cleaned in a mixture of hydrogen peroxide and ammonium hydroxide to remove the Al_2O_3 etch mask, and any etch residues.

Spatiotemporal pulse characterization

<u>*Spectral interferometry:*</u> An ultrafast pulse with a complex time-varying polarization state can be decomposed into the two-constituent *p*- and *s*- polarized components. The temporal evolution of the electric-field vector $\vec{\boldsymbol{E}}_{\text{out}}(t)$ can then be expressed as $\vec{\boldsymbol{E}}_{\text{out}}(t) = \begin{bmatrix} A_p(t)e^{i\Psi_p(t)} \\ A_s(t)e^{i\Psi_s(t)} \end{bmatrix}$, where $A_{p(s)}(t)$ and $\Psi_{p(s)}(t)$ are the temporal amplitude and phase for the *p*- (*s*-) polarized component,

respectively. To characterize $\vec{\boldsymbol{E}}_{\mathrm{out}}(t)$, the spectral phase $\varphi_{p(s)}(\omega)$ and intensity $I_{p(s)}(\omega)$ for the *p*- (*s*-) polarized component are measured separately using the methods described below. The time-domain waveform $\vec{\boldsymbol{E}}_{\mathrm{out}}(t)$ can then be reconstructed from the frequency-domain field $\vec{\boldsymbol{E}}_{\mathrm{out}}(\omega) = \begin{bmatrix} a_p(\omega)e^{i\varphi_p(\omega)} \\ a_s(\omega)e^{i\varphi_s(\omega)} \end{bmatrix}$, through an inverse-Fourier transform operation, where $a_{p(s)}(\omega) = \sqrt{I_{p(s)}(\omega)}$.

The spectral amplitude $a_{p(s)}(\omega)$ of the *p*- (*s*-) polarized component, is characterized by blocking the reference beam and measuring the corresponding spectral intensity $I_{p(s)}(\omega)$. To calculate the normalized spectral amplitudes, an input spectrum $I_0(\omega)$ was also measured by placing only the fused-silica substrate at the Fourier plane.

The spectral phase $\varphi_{p(s)}(\omega)$ for the *p*- (*s*-) polarized component, each containing part of the total pulse energy, is measured using the spectral interferometry (SI) technique (*36*). Nonlinear pulse characterization techniques such as frequency-resolved optical gating (FROG) and spectral interferometry for direct electric-field reconstruction (SPIDER) require high-input powers and are also unable to unambiguously retrieve the constant phase offset (first term in the Taylor series expansion of the spectral phase, ref. *37*), which is required here to accurately determine the instantaneous polarization state of the shaped pulse. To overcome the input-power and phase-offset measurement limitations, SI which only relies on linear optics is leveraged here using a custom-built interferometry setup to characterize the temporal properties of the synthesized pulses. SI retrieves phase information of the shaped pulse by measuring the spectral interference fringes upon interference with a known reference pulse (Fig. 3). Pulses in the experimental beam, which originate after transmission from an ultrafast beam splitter, pass through the pulse shaper and acquire the desired spatiotemporal modulation. The reflected beam, designated as the reference beam, is subsequently delayed by a fixed time τ using a retroreflector mounted on a translation stage, and recombined with the experimental beam using a second ultrafast beam splitter. The combined beams are then directed to the SI measurement setup, where the interference pattern between these two spatially overlapped and temporally sheared pulses is recorded on a spectrometer (Fig. 3, pink inset). A half-wave plate (HWP) and a linear polarizer (LP) in the experimental beam are used to switch between measuring the *p*- and *s*-polarized components, separately. The recorded SI signal $I_{\mathrm{SI}}^{p(s)}(\omega)$ can be expressed as:

$$I_{\mathrm{SI}}^{p(s)}(\omega) = I_{p(s)}(\omega) + I_{\mathrm{ref}}(\omega) + 2\sqrt{I_{p(s)}(\omega)}\sqrt{I_{\mathrm{ref}}(\omega)}\cos\big(\varphi_{p(s)}(\omega) - \varphi_{\mathrm{ref}}(\omega) - \omega\tau_0\big), \quad (5)$$

where $I_{\mathrm{ref}}(\omega)$ and $\varphi_{\mathrm{ref}}(\omega)$ are the spectral intensity and phase of the reference pulse, respectively. Here, τ_0 is the mean extracted value from 1000 measurements of I_{SI}^{p} with only the fused-silica substrate present in the experimental beam path, and the phase difference $(\varphi_{p(s)}(\omega) - \varphi_{\mathrm{ref}}(\omega))$ at this τ_0 is then extracted from the cross-term in Eq. 5 using the fringe inversion technique (*38*). After characterizing $\varphi_{\mathrm{ref}}(\omega)$ using the SPIDER technique (Fig. 3, green inset, and fig. S6), the only remaining unknown $\varphi_{p(s)}(\omega)$ can be retrieved. Note that the path length difference between the SPIDER and the SI measurement setup was measured to be ≈9 cm, which corresponds to a group delay dispersion in air of ≈1.8 fs^2/rad, resulting in negligible broadening of the input pulse.

Spatial interferometry: Characterizing the time-varying spatial profile of the shaped pulse involves determining the time-dependent spatial phase $\Psi_{p(s)}(x, y, t)$ and amplitude $A_{p(s)}(x, y, t)$ of the *p*- (*s*-) polarized component at different time-delays $t = \tau$, which is achieved by performing spatial interferometry between the experimental beam and a transform-limited reference beam that carries

a Gaussian spatial profile with a quasi-flat phase front. A small tilt angle between the wavefronts of the reference and experimental beams is introduced to create fringe interference patterns. The interference fringes are recorded on a CMOS sensor for various values of τ. By counting the number of fringe-dislocations and comparing their orientations, the topological charge of $\Psi_{p(s)}(x, y, \tau)$ at different τ can be determined. The spatial amplitude $A_{p(s)}(x, y, t)$, on the other hand, is proportional to the oscillation amplitude of the cross-term between experimental and reference fields, *i.e.*, the contrast of the bright and dark fringes. Further details on evaluating the time-varying spatial amplitude are discussed in Supplementary Text S5.

The time-averaged spatial amplitude $\bar{A}_{p(s)}(x, y)$ of the p- (s-) polarized component is directly characterized by blocking the reference beam and recording the corresponding spatial intensity distribution $\bar{I}_{p(s)}(x, y) = \bar{A}^2_{p(s)}(x, y)$ on the CMOS sensor.

REFERENCES AND NOTES

1. N. Dudovich, D. Oron, Y. Silberberg, Single-pulse coherently controlled nonlinear Raman spectroscopy and microscopy. *Nature* **418**, 512-514 (2002).

2. T. Brixner, F. J. García de Abajo, J. Schneider, W. Pfeiffer, Nanoscopic ultrafast space-time-resolved spectroscopy. *Phys. Rev. Lett.* **95**, 093901 (2005).

3. M. Aeschlimann, M. Bauer, D. Bayer, T. Brixner, S. Cunovic, F. Dimler, A. Fischer, W. Pfeiffer, M. Rohmer, C. Schneider, F. Steeb, C. Strüber, D. V. Voronine, Spatiotemporal control of nanooptical excitations. *Proc. Natl. Acad. Sci.* **107**, 5329-5333 (2010).

4. P. Hommelhoff, M. Kling, *Attosecond Nanophysics: From Basic Science to Applications*. (John Wiley & Sons, 2015).

5. National Academies of Sciences, Engineering, and Medicine, *Opportunities in Intense Ultrafast Lasers: Reaching for the Brightest Light* (The National Academies Press, Washington, DC, 2018).

6. R. Thomson, C. Leburn, D. Reid, Eds., *Ultrafast Nonlinear Optics* (Springer, 2013).

7. T. Südmeyer, S. V. Marchese, S. Hashimoto, C. R. E. Baer, G. Gingras, B. Witzel, U. Keller, Femtosecond laser oscillators for high-field science. *Nat. Photonics* **2**, 599-604 (2008).

8. A. J. Metcalf, T. Anderson, C. F. Bender, S. Blakeslee, W. Brand, D. R. Carlson, W. D. Cochran, S. A. Diddams, M. Endl, C. Fredrick, S. Halverson, D. D. Hickstein, F. Hearty, J. Jennings, S. Kanodia, K. F. Kaplan, E. Levi, E. Lubar, S. Mahadevan, A. Monson, J. P. Ninan, C. Nitroy, S. Osterman, S. B. Papp, F. Quinlan, L. Ramsey, P. Robertson, A. Roy, C. Schwab, S. Sigurdsson, K. Srinivasan, G. Stefansson, D. A. Sterner, R. Terrien, A. Wolszczan, J. T. Wright, G. Ycas, Stellar spectroscopy in the near-infrared with a laser frequency comb. *Optica* **6**, 233-239 (2019).

9. N. Picqué, T. W. Hänsch, Frequency comb spectroscopy. *Nat. Photonics* **13**, 146-157 (2019).

10. S. A. Diddams, K. Vahala, T. Udem, Optical frequency combs: Coherently uniting the electromagnetic spectrum. *Science* **369**, eaay3676 (2020).

11. J. X. Tull, M. A. Dugan, W. S. Warren, High-resolution, ultrafast laser pulse shaping and its applications. *Advances in Magnetic and Optical Resonance* **20**, 1 (1997).

12. A. M. Weiner, Ultrafast optical pulse shaping: A tutorial review. *Opt. Commun.* **284**, 3669-3692 (2011).

13. D. Strickland, G. Mourou, Compression of amplified chirped optical pulses. *Opt. Commun.* **55**, 447-449 (1985).

14. S. T. Cundiff, A. M. Weiner, Optical arbitrary waveform generation. *Nat. Photonics* **4**, 760-766 (2010).

15. M. Yessenov, L. A. Hall, K. L. Schepler, A. F. Abouraddy, Space-time wave packets, http://arxiv.org/abs/2201.08297 (2022).

16. A. H. Dorrah, F. Capasso, Tunable structured light with flat optics. *Science* **376**, eabi6860 (2022).

17. A. Korobenko, A. A. Milner, J. W. Hepburn, V. Milner, Rotational spectroscopy with an optical centrifuge. *Phys. Chem. Chem. Phys.* **16**, 4071-4076 (2014).

18. M. Padgett, R. Bowman, Tweezers with a twist. *Nat. Photonics* **5**, 343-348 (2011).

19. Y. Dai, Z. Zhou, A. Ghosh, R. S. K. Mong, A. Kubo, C.-B. Huang, H. Petek, Plasmonic topological quasiparticle on the nanometre and femtosecond scales. *Nature* **588**, 616-619 (2020).

20. J. W. McIver, D. Hsieh, H. Steinberg, P. Jarillo-Herrero, N. Gedik, Control over topological insulator photocurrents with light polarization. *Nat. Nanotechnol.* **7**, 96-100 (2012).

21. F. Kong, C. Zhang, F. Bouchard, Z. Li, G. G. Brown, D. H. Ko, T. J. Hammond, L. Arissian, R. W. Boyd, E. Karimi, P. B. Corkum, Controlling the orbital angular momentum of high harmonic vortices. *Nat. Commun.* **8**, 14970 (2017).

22. L. Rego, K. M. Dorney, N. J. Brooks, Q. L. Nguyen, C.-T. Liao, J. San Román, D. E. Couch, A. Liu, E. Pisanty, M. Lewenstein, L. Plaja, H. C. Kapteyn, M. M. Murnane, C. Hernández-García, Generation of extreme-ultraviolet beams with time-varying orbital angular momentum. *Science* **364**, eaaw9486 (2019).

23. T. Fan, P. Grychtol, R. Knut, C. Hernández-García, D. D. Hickstein, D. Zusin, C. Gentry, F. J. Dollar, C. A. Mancuso, C. W. Hogle, O. Kfir, D. Legut, K. Carva, J. L. Ellis, K. M. Dorney, C. Chen, O. G. Shpyrko, E. E. Fullerton, O. Cohen, P. M. Oppeneer, D. B. Milošević, A. Becker, A. A. Jaroń-Becker, T. Popmintchev, M. M. Murnane, H. C. Kapteyn, Bright circularly polarized soft X-ray high harmonics for X-ray magnetic circular dichroism. *Proc. Natl. Acad. Sci.* **112**, 14206-14211 (2015).

24. L. Rego, N. J. Brooks, Q. L. D. Nguyen, J. San Román, I. Binnie, L. Plaja, H. C. Kapteyn, M .M. Murnane, C. Hernández-García, Necklace-structured high-harmonic generation for low-divergence, soft x-ray harmonic combs with tunable line spacing. *Sci. Adv.* **8**, eabj7380 (2022).

25. Z. Zhao, H. Song, R. Zhang, K. Pang, C. Liu, H. Song, A. Almaiman, K. Manukyan, H. Zhou, B. Lynn, R. W. Boyd, M. Tur, A. E. Willner, Dynamic spatiotemporal beams that combine two independent and controllable orbital-angular-momenta using multiple optical-frequency-comb lines. *Nat. Commun.* **11**, 4099 (2020).

26. G. Pariente, F. Quéré, Spatio-temporal light springs: extended encoding of orbital angular momentum in ultrashort pulses. *Opt. Lett.* **40**, 2037-2040 (2015).

27. S. Fu, Y. Zhai, J. Zhang, X. Liu, R. Song, H. Zhou, C. Gao, Universal orbital angular momentum spectrum analyzer for beams. *PhotoniX* **1**, 19 (2020).

28. A. Forbes, M. de Oliveira, M. R. Dennis, Structured light. *Nat. Photonics* **15**, 253-262 (2021).

29. D. H. Froula, D. Turnbull, A. S. Davies, T. J. Kessler, D. Haberberger, J. P. Palastro, S.-W. Bahk, I. A. Begishev, R. Boni, S. Bucht, J. Katz, J. L. Shaw, Spatiotemporal control of laser intensity. *Nat. Photonics* **12**, 262-265 (2018).

30. A. Chong, C. Wan, J. Chen, Q. Zhan, Generation of spatiotemporal optical vortices with controllable transverse orbital angular momentum. *Nat. Photonics* **14**, 350-354 (2020).

31. B. E. Schmidt, P. Lassonde, G. Ernotte, M. Clerici, R. Morandotti, H. Ibrahim, F. Légaré, Decoupling frequencies, amplitudes and phases in nonlinear optics. *Sci. Rep.*, **7**, 7861 (2017).

32. J. Yang, S. Gurung, S. Bej, P. Ni, and H. W. H. Lee, Active optical metasurfaces: comprehensive review on physics, mechanisms, and prospective applications, *Rep. Prog. Phys.* **85**, 036101 (2022).

33. S. Divitt, W. Zhu, C. Zhang, H. J. Lezec, A. Agrawal, Ultrafast optical pulse shaping using dielectric metasurfaces. *Science* **364**, 890 (2019).

34. Y. Yang, W. Wang, A. Boulesbaa, I. I. Kravchenko, D. P. Briggs, A. Puretzky, D. Geohegan, J. Valentine, Nonlinear Fano-resonant dielectric metasurfaces. *Nano Lett.* **15**, 7388-7393 (2015).

35. V. Liu, S. Fan, S^4 : A free electromagnetic solver for layered periodic structures. *Comput. Phys. Commun.* **183**, 2233-2244 (2012).

36. W. J. Walecki, D. N. Fittinghoff, A. L. Smirl, R. Trebino, Characterization of the polarization state of weak ultrashort coherent signals by dual-channel spectral interferometry. *Opt. Lett.* **22**, 81-83 (1997).

37. A. Monmayrant, S. Weber, B. Chatel, A newcomer's guide to ultrashort pulse shaping and characterization. *J. Phys. B: At. Mol. Opt. Phys.* **43**, 103001 (2010).

38. L. Lepetit, G. Chériaux, M. Joffre, Linear techniques of phase measurement by femtosecond spectral interferometry for applications in spectroscopy. *J. Opt. Soc. Am. B* **12**, 2467-2474 (1995).

39. M. B. Danailov, I. P. Christov, Time-space shaping of light pulses by Fourier optical processing. *J. Mod. Opt.* **36**, 725-731 (1989).

40. A. M. Yao, M. J. Padgett, Orbital angular momentum: origins, behavior and applications. *Adv. Opt. Photonics* **3**, 161-204 (2011).

Acknowledgements: The authors thank A. Chanana, S. Divitt, J. Strait, P. Vabishchevich, and O. Koksal for valuable discussions.

Funding: L.C. and W.Z. acknowledge support under the Cooperative Research Agreement between the University of Maryland and NIST-PML, Award no. 70NANB10H193.

Author contributions: All authors contributed to the design of the experiments. The measurements were performed by L.C., W.Z., and A.A. Simulations were performed by L.C., W.Z., and P.H. with further analysis by H.J.L., T.X., and A.A. Device fabrication were performed by W.Z. and J.S. All authors contributed to the interpretation of results and participated in manuscript preparation.

Competing interests: The authors declare that they have no competing interests.

Data and materials availability: All data needed to evaluate the conclusions in the paper are available in the manuscript or the Supplementary Materials.

Supplementary Materials

Supplementary Text S1 – S6
Figs. S1 to S11
Movies S1 – S2

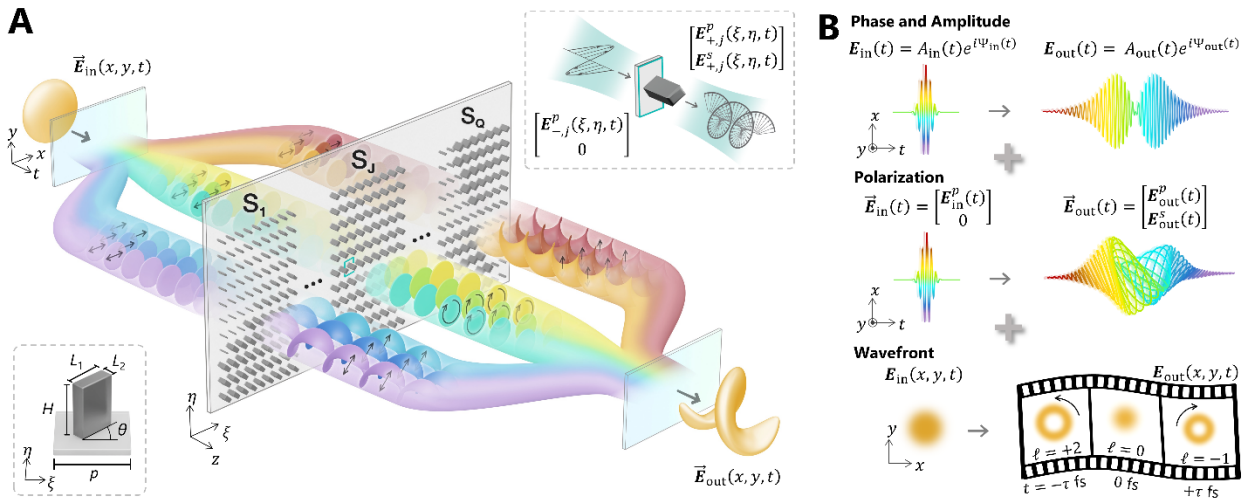

Figure 1. Synthesis of ultrafast optical pulses with arbitrary spatiotemporal control enabled by a dielectric metasurface. (**A**) Schematic of the spatiotemporal Fourier-transform pulse synthesizer, with a single-layer transmission-mode metasurface consisting of Q contiguous superpixels, labeled as S_J ($J = 1, 2, \dots Q$), placed at the Fourier-plane. Spatially dispersed frequency components of an incoming linearly polarized optical pulse with Gaussian spatial distribution, upon interaction with the corresponding S_J, are simultaneously transformed into targeted waveforms with the requisite amplitude, phase, polarization and wavefront distribution, and coherently recombined. Bottom left inset: Schematic perspective view of a metasurface unit cell (pitch size p) consisting of a dielectric nanopillar of height H and in-plane dimensions L_1 and L_2, placed at a rotation angle θ. Top right inset: One representative metasurface unit cell (cyan outline in S_J) acting as a quarter-wave plate. (**B**) Simultaneous and independent control of the instantaneous phase, amplitude, polarization and wavefront as a function of time enabled by the pulse synthesizer.

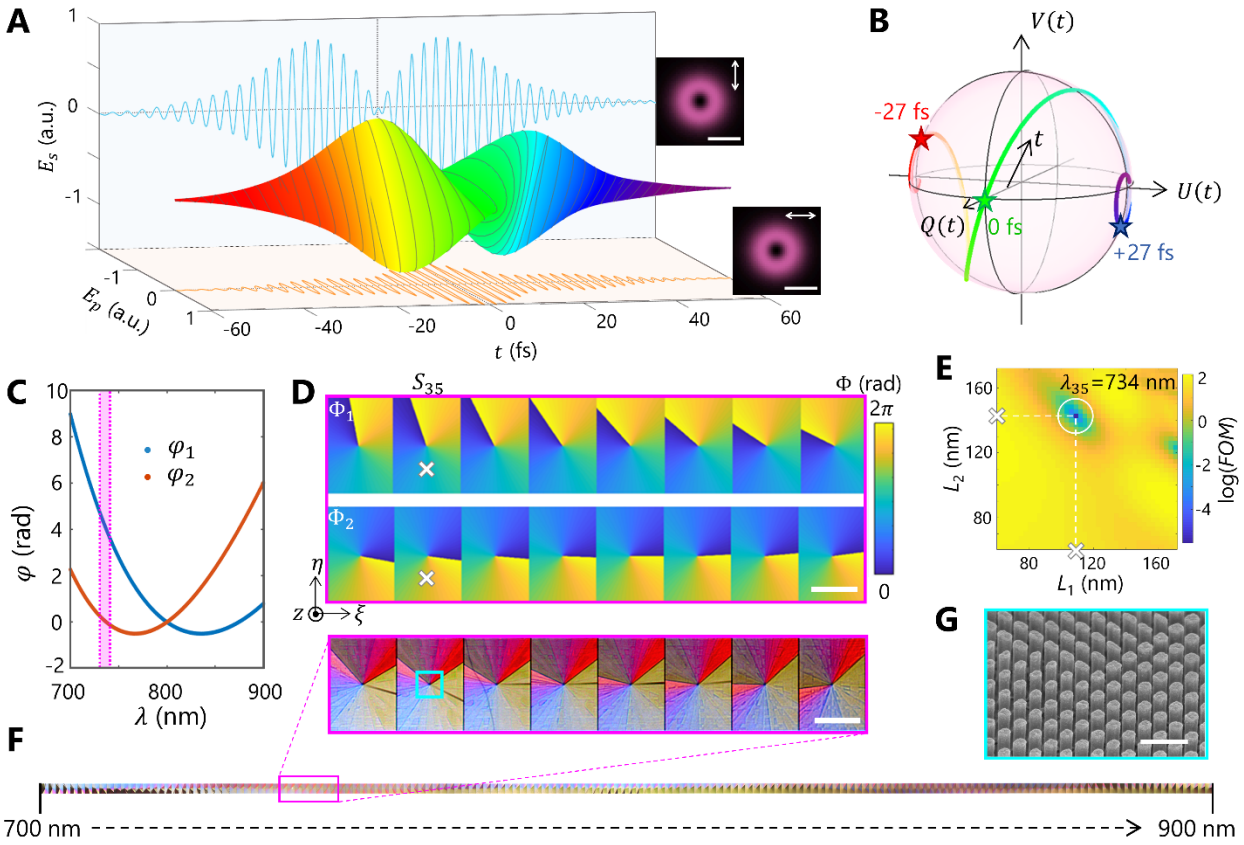

Figure 2. Metasurface design to synthesize an OAM-carrying, polarization-swept ultrafast pulse. (**A**) Numerically simulated three-dimensional electric-field representation of the targeted pulse assuming the carrier-envelope-phase to be zero. Grey solid line overlaid on the surface of the pulse tracks the tip of the instantaneous electric-field vector *vs.* t. Orange and blue projections represent the *p*- and *s*-polarized electric-field components, respectively. Insets: simulated output intensity distribution of the synthesized pulse carrying an OAM order of $\ell = -1$ for the *p*- and *s*-polarized components. Scale bars: 5 mm. (**B**) Poincaré sphere representation of the time-varying polarization state in (A). $Q(t)$, $U(t)$, $V(t)$ correspond to the Stokes parameters, and are defined in Supplementary Text, S6. Red, green, and blue stars mark three representative instantaneous polarization states at –27 fs, 0 fs, and +27 fs, respectively. (**C**) Targeted spectral phase $\varphi_{1(2)}$ *vs.* λ. (**D**) Targeted phase topographies Φ_1 and Φ_2 for eight representative superpixels within the pink-shaded spectral region in (C). Scale bar: 100 μm. (**E**) Figure of merit (*FOM*) *vs*. nanopillar in-plane dimensions (L_1, L_2), plotted in logarithmic scale for $\lambda_J = 734$ nm. The local *FOM* minima (white circle) yields a combination of L_1 and L_2 (white crosses) that simultaneously satisfies the targeted phases $\Phi_1 = 0.90\pi$ and $\Phi_2 = 1.54\pi$ for one nanopillar location within the superpixel at $\lambda_J = 734$ nm (white crosses in D), while offering the highest transmittance along the two nanopillar axes. (**F**) Optical transmission image of the fabricated metasurface under unpolarized white light illumination. Inset: magnified image of eight superpixels corresponding to the phase-maps in (C). Scale bar: 100 μm. (**G**) Representative SEM image of the nanopillars (perspective view at 52°) taken at position marked by the cyan box in the magnified image in (F). Scale bar: 500 nm.

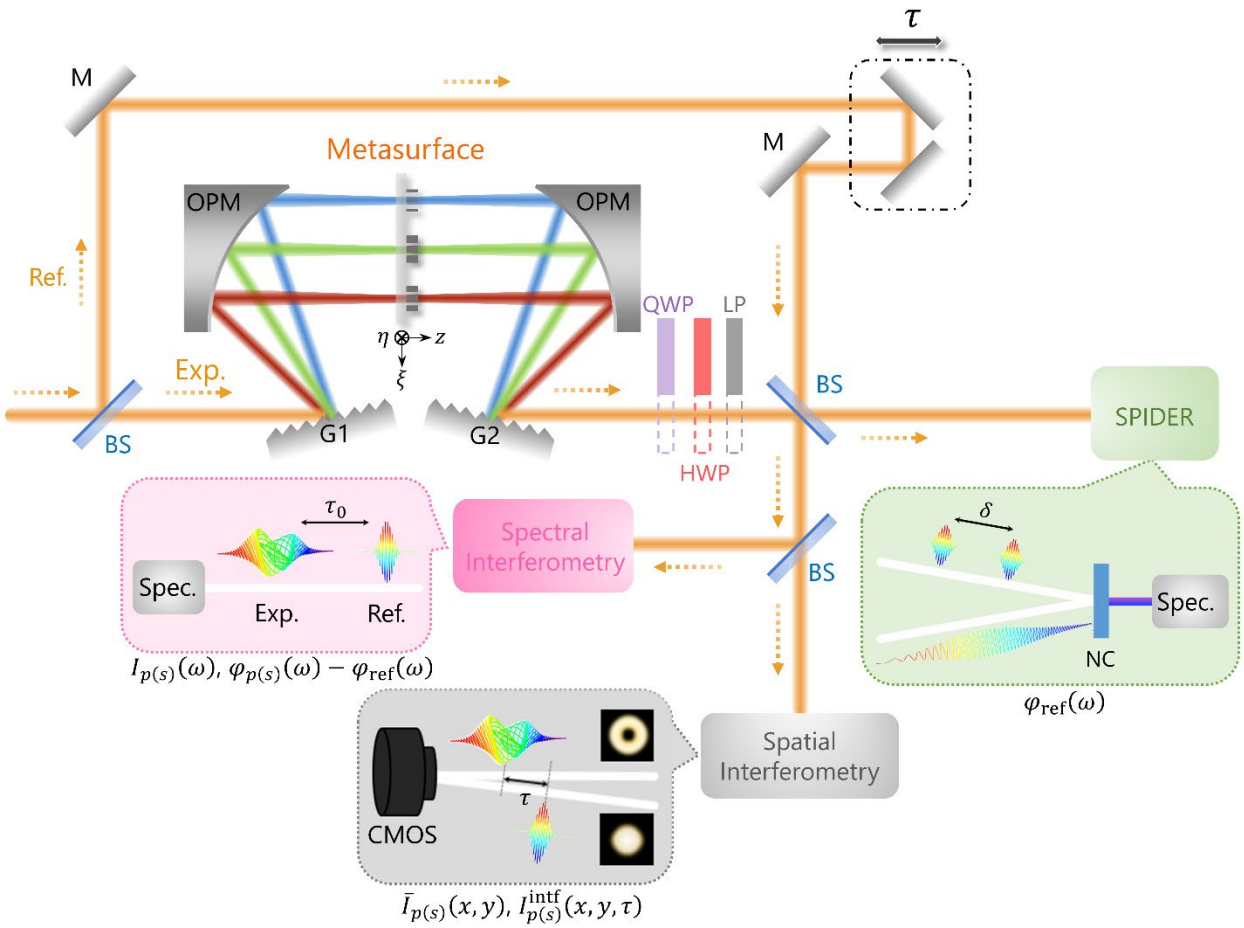

Figure 3. Schematic diagram of the experimental setup. The experimental beam (labelled: Exp.) propagates through the pulse shaper and acquires a targeted spatiotemporal modulation. The reference beam (labelled: Ref.) is delayed by τ with respect to Exp. beam to perform spatial and spectral interferometry (grey and pink inset, respectively) on the shaped pulses, and is also independently characterized by the spectral phase interferometry for direct electric-filed reconstruction (SPIDER) method (green inset). BS: beam splitter, M: mirror, G1 and G2: grating, OPM: off-axis parabolic mirror, HWP: half-wave plate, QWP: quarter-wave plate, LP: linear polarizer, NC: nonlinear crystal, Spec.: spectrometer. Pink inset: polarization resolved temporal pulse reconstruction using spectral interferometry (SI). Grey inset: polarization resolved time-varying spatial wavefront reconstruction using spatial interferometry. Green inset: SPIDER technique based on spectral shearing interferometry.

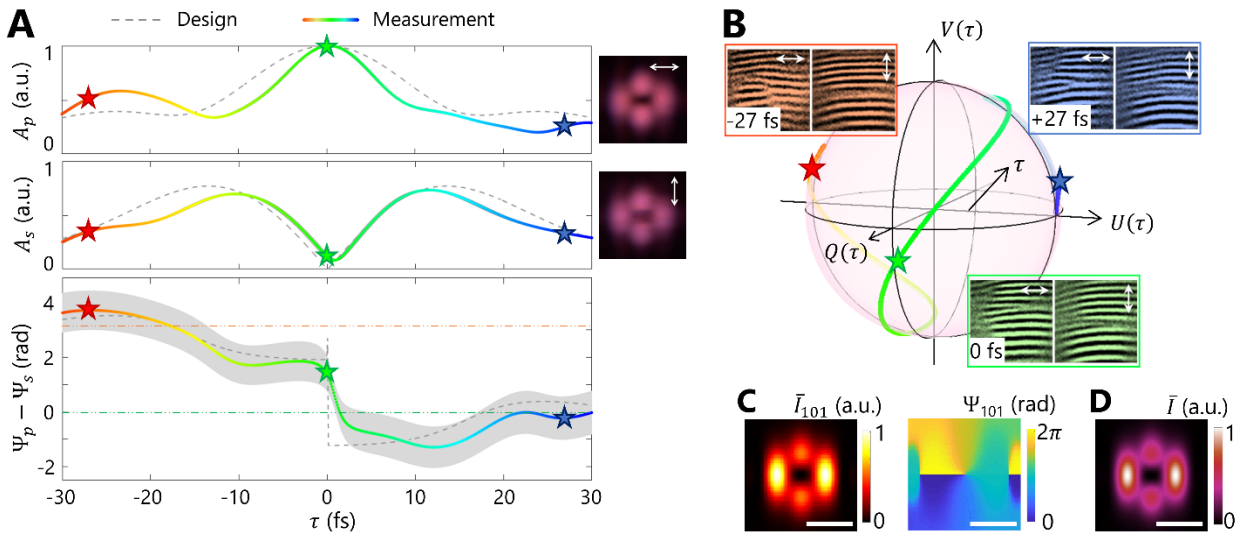

Figure 4. Experimental implementation of an OAM-carrying, polarization-swept ultrafast pulse. (**A**) Temporal amplitudes $A_p(\tau)$ (top), $A_s(\tau)$ (middle), and phase difference $\Psi_p(\tau) - \Psi_s(\tau)$ (bottom) of the designed (grey dashed lines) and measured (solid colored lines) pulse illustrating the rich set of time-varying polarization states endowed to the pulse. The surrounding shadows represent one standard deviation from 1000 measurements. Colored dashed lines in the bottom plot denote 0 (green) and π (orange), respectively. Inset camera images show the measured $\bar{I}_{\text{out}}^{p(s)}$. (**B**) The measured time-varying polarization state of the shaped pulse represented as a trace on the Poincaré sphere. Insets: representative spatial interferometry images for the p- and s-polarization, all exhibiting an OAM order of $\ell = -1$, measured at $\tau = -27$ fs, 0 fs, and $+27$ fs. (**C**) Simulated $\bar{I}_{\text{out},101}^{p}$ (left) and $\Psi_{\text{out},101}^{p}$ (right) accounting for all 6250 spectral lines illuminating one representative superpixel (S_{101}). (**D**) Simulated collective output intensity distribution of the synthesized pulse $\vec{E}_{\text{out}}(x, y, t)$ carrying an OAM order of $\ell = -1$, closely matching the measured intensity distribution in (A). Scale bars in (C) and (D): 5 mm.

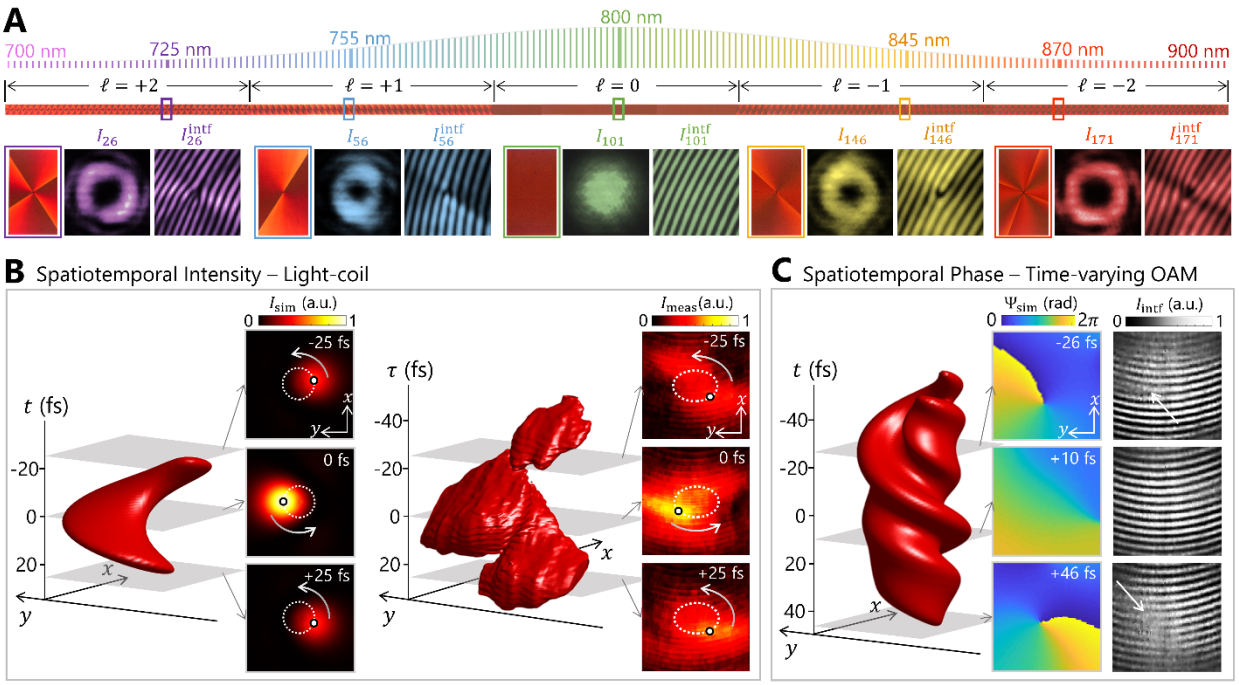

Figure 5. Synthesis of an ultrafast light-coil and a spatiotemporal pulse carrying time-varying OAM. (**A**) Five OAM orders $\ell_J = +2, +1, 0, -1$ and -2 are assigned to each superpixel within a set of five spectral sub-regions. Top: schematic spectral intensity distribution at frequencies ω_J of the input femtosecond pulse. Middle: optical transmission image of the fabricated metasurface designed to impart the targeted OAM orders to each $\Delta\lambda_J$. Bottom: magnified image (left) of five representative superpixels S_J ($J = 26, 56, 101, 146, 171$), along with the corresponding transmitted intensity distribution I_J (middle) and spatial interferogram I_J^{intf} (right) measured at corresponding λ_J. (**B**) Simulated (left) and experimentally reconstructed (right) spatiotemporal wave packet for the synthesized light-coil. The plots show iso-intensity profile at 40 % and 50 % of the peak intensity, respectively. Left (right) insets: instantaneous simulated (reconstructed) intensity distribution I_{sim} (I_{meas}) at three representative time delays $\tau = -25$ fs, 0 fs, and $+25$ fs. (**C**) Simulated spatiotemporal wave packet carrying time-varying OAM (left). The plot shows iso-intensity profile at 10% of the peak intensity. Simulated phase profile Ψ_{sim} (middle) and measured spatial interferometry I_{intf} (right) at $\tau = -26$ fs, 10 fs, and $+46$ fs, respectively. White arrows indicate fork-dislocations in the interference fringes with opposite openings.

Supplementary Materials for

Synthesizing ultrafast optical pulses with arbitrary spatiotemporal control

Lu Chen[1,2,*], Wenqi Zhu[1,2], Pengcheng Huo[3], Junyeob Song[1], Henri J. Lezec[1], Ting Xu[3] and Amit Agrawal[1,*]

[1]National Institute of Standards and Technology, Gaithersburg, MD 20899, USA

[2]University of Maryland, College Park, MD 20742, USA

[3]College of Engineering and Applied Physics, Nanjing University, Nanjing 210093, China

*Corresponding authors. e-mail: lu.chen@nist.gov, amit.agrawal@nist.gov

This PDF file includes:

Other Supplementary Materials for this manuscript include the following:

Movies S1 and S2

S1. Spatiotemporal shaping of ultrafast pulses: separating spatial and temporal masking functions

An input femtosecond pulse train in the time-domain is equivalent to a series of equally spaced spectral lines at frequencies ν_j (j is an integer) in the frequency domain. The corresponding angular frequencies are expressed as, $\omega_j = 2\pi\nu_j = 2\pi(j\nu_{\mathrm{rep}} + \nu_0)$, where ν_{rep} is the repetition rate of the pulse train and ν_0 is the offset frequency. Assuming an input beam with Gaussian spatial distribution, the transform-limited electric field $\vec{\boldsymbol{E}}_{\mathrm{in}}$ of a p-polarized (electric-field oscillating along the x-direction) input pulse train can be expressed by its Fourier series:

$$\vec{\boldsymbol{E}}_{\mathrm{in}}(x,y,t) = \sum_j E(x)E(y)\boldsymbol{E}(\omega_j,t)\begin{bmatrix}1\\0\end{bmatrix} = \sum_j e^{-\frac{x^2}{\sigma^2}}e^{-\frac{y^2}{\sigma^2}}a_j e^{-i\omega_j t}\begin{bmatrix}1\\0\end{bmatrix}, \tag{S1}$$

where spatial components $E(x)$, $E(y)$ and temporal components $\boldsymbol{E}(\omega_j,t)$ are treated as separable variables, σ is the spatial beam-waist radius, a_j is the spectral amplitude, and $\begin{bmatrix}1\\0\end{bmatrix}$ is the Jones vector that represents the input polarization state.

In the Fourier transform pulse shaper (Fig. 3), the input grating diffracts each frequency component ω_j into a specific angle exiting the x-y plane. Without losing generality, the effect of the grating is to add a linear phase to the input field along the x-direction, resulting in a field $\vec{\boldsymbol{E}}_{\mathrm{G1}}$ at the exit of the input grating expressed as:

$$\vec{\boldsymbol{E}}_{\mathrm{G1}}(x,y,t) = \mathcal{G}\{\vec{\boldsymbol{E}}_{\mathrm{in}}(x,y,t)\} = \sum_j E(x)e^{\frac{i2\pi x}{\Lambda_{\mathrm{G}}}}E(y)a_j e^{-i\omega_j t}\begin{bmatrix}1\\0\end{bmatrix}, \tag{S2}$$

where $\mathcal{G}$ represents the grating function and Λ_{G} is the grating pitch. A comprehensive derivation leading to the same results can be performed by following the approach presented in ref. *39*.

Next, the angularly dispersed spectral components are focused by an off-axis parabolic mirror onto the metasurface placed at the Fourier plane (defined as the ξ-η plane) in a 2-f configuration. The electric field in the ξ-η plane at the input of the metasurface, $\vec{\boldsymbol{E}}_{-}(\xi,\eta,t)$, is the spatial Fourier transform of $\vec{\boldsymbol{E}}_{\mathrm{G1}}(x,y,t)$:

$$\vec{\boldsymbol{E}}_{-}(\xi,\eta,t) = \mathcal{F}|_{xy\to\xi\eta}\{\vec{\boldsymbol{E}}_{\mathrm{G1}}(x,y,t)\} = \sum_j u_j(\xi-\xi_j)u_j(\eta)a_j e^{-i\omega_j t}\begin{bmatrix}1\\0\end{bmatrix}. \tag{S3}$$

Here, $\xi_j = (\lambda_j - \lambda_{\mathrm{c}})f/\Lambda_{\mathrm{G}}$, and $u_j(\xi)$ is the one-dimensional (1D) spatial Fourier transform of the Gaussian spot for the spectral line ν_j, given by:

$$u_j(\xi) = \mathcal{F}|_{x\to\xi}\left\{e^{-\frac{x^2}{\sigma^2}}\right\} = e^{-\left(\frac{\xi}{w_j}\right)^2}, \tag{S4}$$

where $w_j = \lambda_j f/\pi\sigma$ is the diffraction-limited beam waist of the spectral line ν_j at the Fourier plane.

In the following, we show that polarization-multiplexed, spatiotemporal pulse shaping can be achieved by using the metasurface design scheme described below. Note that $\vec{\boldsymbol{E}}_-(\xi,\eta,t)$ is the summation of a 1D array of diffraction-limited, quasi continuous-wave (cw) Gaussian spots, representing a beam consisting of different spectral lines spatially dispersed along the ξ-axis at the Fourier plane. The Jones matrix of the metasurface $\boldsymbol{M}(\xi,\eta)$ can be written as a complex 2×2 matrix; hence, the electric field distribution of the beam after passing through the metasurface $\vec{\boldsymbol{E}}_+(\xi,\eta,t)$ is given by:

$$\begin{aligned}\vec{\boldsymbol{E}}_+(\xi,\eta,t) &= \begin{bmatrix}\boldsymbol{E}_+^p(\xi,\eta,t)\\ \boldsymbol{E}_+^s(\xi,\eta,t)\end{bmatrix} = \boldsymbol{M}(\xi,\eta)\vec{\boldsymbol{E}}_-(\xi,\eta,t)\\ &= \begin{bmatrix}\boldsymbol{M}_{11} & \boldsymbol{M}_{12}\\ \boldsymbol{M}_{21} & \boldsymbol{M}_{22}\end{bmatrix}\boldsymbol{E}_-(\xi,\eta,t)\begin{bmatrix}1\\0\end{bmatrix}\\ &\triangleq \begin{bmatrix}\boldsymbol{M}_p(\xi,\eta)\boldsymbol{E}_-(\xi,\eta,t)\\ \boldsymbol{M}_s(\xi,\eta)\boldsymbol{E}_-(\xi,\eta,t)\end{bmatrix}.\end{aligned} \tag{S5}$$

The detailed implementation of the four elements of $\boldsymbol{M}(\xi,\eta)$, representing a polarization multiplexing functionality, is described in section S3. Here, we take $\boldsymbol{M}_p(\xi,\eta)$ as an example. Note that $\xi_j \propto \lambda_j$; we design a metasurface consisting of $Q = 201$ superpixels, each nominally manipulating a $\Delta\lambda \approx 1$ nm bandwidth of the pulse spectrum ranging from 700 nm to 900 nm. For each $J \in [1, Q]$, the J-th superpixel, centered at $\xi_J = (\lambda_J - \lambda_c)f/\Lambda_G$, simultaneously imparts a targeted spectral modulation $\boldsymbol{\Upsilon}_J^p(\omega_J)$, which is spatially constant across each superpixel, and a targeted spatial modulation $\boldsymbol{\Gamma}_J^p(\xi,\eta)$, varying within each superpixel, on the subgroup of spectral lines centered at wavelength $\lambda_J = (699 + J)$ nm.The targeted masking function of the metasurface $\boldsymbol{M}_p(\xi,\eta)$ can be expressed as a two-dimensional (2D) concatenated function:

$$\boldsymbol{M}_p(\xi,\eta) = \sum_{J=1}^{Q}\boldsymbol{\Upsilon}_J^p(\omega_J)\boldsymbol{\Gamma}_J^p(\xi-\xi_J,\eta)\Pi(\xi-\xi_J). \tag{S6}$$

Here, $\Pi(\xi)$ is a rectangular function defined as:

$$\Pi(\xi) = \begin{cases}1, & -\dfrac{D}{2} \le \xi < \dfrac{D}{2},\\ 0, & \text{else}\end{cases} \tag{S7}$$

where $D = f\Delta\lambda/\Lambda_G$ is the width of the superpixel.

To further simplify $\boldsymbol{E}_+^p(\xi,\eta,t)$, noting $\Delta\xi_j \ll w_j$, given Q is large and the input spectrum is slow-varying, $\boldsymbol{E}_-(\xi,\eta,t)$ can be resampled with Q spectral lines and expressed as:

$$\begin{aligned}\boldsymbol{E}_{-}(\xi,\eta,t) &= \sum_{j} u_j(\xi-\xi_j)u_j(\eta)a_j e^{-i\omega_j t} \\ &= \sum_{J=1}^{Q}\left(\sum_{\lambda_J-\frac{\Delta\lambda_J}{2}\le\lambda_j<\lambda_J+\frac{\Delta\lambda_J}{2}} u_j(\xi-\xi_j)u_j(\eta)a_j e^{-i\omega_j t}\right) \\ &\approx \sum_{J=1}^{Q} a_J\Pi(\xi-\xi_J)u_J(\eta)e^{-i\omega_J t},\end{aligned} \tag{S8}$$

With this approximation, we have:

$$\begin{aligned}\boldsymbol{E}_{+}^{p}(\xi,\eta,t) &= \boldsymbol{M}_p(\xi,\eta)\boldsymbol{E}_{-}(\xi,\eta,t) \\ &= \left\{\sum_{J=1}^{Q}\boldsymbol{\Upsilon}_J^p(\omega_J)\boldsymbol{\Gamma}_J^p(\xi-\xi_J,\eta)\Pi(\xi-\xi_J)\right\}\left\{\sum_{J=1}^{Q}a_J\Pi(\xi-\xi_J)u_J(\eta)e^{-i\omega_J t}\right\} \\ &= \sum_{J=1}^{Q}\{a_J\boldsymbol{\Upsilon}_J^p(\omega_J)e^{-i\omega_J t}\}\{\boldsymbol{\Gamma}_J^p(\xi-\xi_J,\eta)\Pi(\xi-\xi_J)u_J(\eta)\}\end{aligned} \tag{S9}$$

Going back to the 4-f configuration, the second identical off-axis parabolic mirror performs the inverse spatial Fourier transform on the modulated $\boldsymbol{E}_{+}^{p}(\xi,\eta,t)$, resulting in the field $\vec{\boldsymbol{E}}_{\mathrm{G2}}$ at the input of the second grating, expressed as:

$$\begin{aligned}\boldsymbol{E}_{\mathrm{G2}}^{p}(x,y,t) &= \mathcal{F}^{-1}|_{\xi\eta\to xy}\{\boldsymbol{E}_{+}^{p}(\xi,\eta,t)\} \\ &= \sum_{J=1}^{Q} a_J\boldsymbol{\Upsilon}_J^p(\omega_J)e^{-i\omega_J t}\mathcal{F}^{-1}\{\boldsymbol{\Gamma}_J^p(\xi-\xi_J,\eta)\Pi(\xi-\xi_J)u_J(\eta)\} \\ &= \sum_{J=1}^{Q} a_J\boldsymbol{\Upsilon}_J^p(\omega_J)e^{-i\omega_J t}\mathcal{F}^{-1}\{\boldsymbol{\Gamma}_J^p(\xi,\eta)\Pi(\xi)u_J(\eta)\}e^{\frac{i2\pi\xi_J x}{\lambda_J f}}.\end{aligned} \tag{S10}$$

Finally, the second grating recombines the angularly dispersed electric fields in Eq. S10, resulting in a train of spatiotemporally shaped output pulses, with $\boldsymbol{E}_{\mathrm{out}}^{p}(x,y,t)$ expressed as:

$$\boldsymbol{E}_{\mathrm{out}}^{p}(x,y,t) = \sum_{J=1}^{Q} a_J\boldsymbol{\Upsilon}_J^p(\omega_J)e^{-i\omega_J t}\mathcal{F}^{-1}\{\boldsymbol{\Gamma}_J^p(\xi,\eta)\Pi(\xi)u_J(\eta)\}e^{\frac{i2\pi\xi_J x}{\lambda_J f}}e^{-i\frac{2\pi}{\Lambda_{\mathrm{G}}}x} \tag{S11}$$

$$= \sum_{J=1}^{Q} a_J \boldsymbol{\Upsilon}_J^p(\omega_J) e^{-i\omega_J t} \mathcal{F}^{-1}\{\boldsymbol{\Gamma}_J^p(\xi,\eta)\Pi(\xi)u_J(\eta)\}$$

$$\triangleq \sum_{J=1}^{Q} \boldsymbol{E}_{\text{out},J}^p(\omega_J, t)\boldsymbol{E}_{\text{out},J}^p(x,y).$$

Following the same procedure for the *s*-polarization, the full output electric field can be expressed as:

$$\vec{\boldsymbol{E}}_{\text{out}}(x,y,t) = \begin{bmatrix} \boldsymbol{E}_{\text{out}}^p(x,y,t) \\ \boldsymbol{E}_{\text{out}}^s(x,y,t) \end{bmatrix} = \begin{bmatrix} \sum_{J=1}^{Q} \boldsymbol{E}_{\text{out},J}^p(\omega_J, t)\boldsymbol{E}_{\text{out},J}^p(x,y) \\ \sum_{J=1}^{Q} \boldsymbol{E}_{\text{out},J}^s(\omega_J, t)\boldsymbol{E}_{\text{out},J}^s(x,y) \end{bmatrix} \tag{S12}$$

S2. Jones Calculus for Polarization Multiplexing

In section S1, we denote the Jones matrix of each polarization-multiplexed metasurface $\boldsymbol{M}(\xi,\eta)$ to be a complex 2×2 term, given by $\boldsymbol{M}(\xi,\eta) = \begin{bmatrix} \boldsymbol{M}_p(\xi,\eta) & \boldsymbol{M}_{12} \\ \boldsymbol{M}_s(\xi,\eta) & \boldsymbol{M}_{22} \end{bmatrix}$ (Eq. S5). Here, given a targeted $\boldsymbol{M}_p(\xi,\eta)$ and $\boldsymbol{M}_s(\xi,\eta)$, we describe the metasurface design process for each pixel. The polarization multiplexing function at the single pixel level is achieved via a dielectric nanopillar of rectangular cross-section acting as a birefringent waveplate providing phase-shifts Φ_1 and Φ_2 for light polarized along its major and minor axes. When rotated counter-clockwise with respect to the *x*-direction by an angle θ, the Jones matrix of the birefringent nanopillar can be expressed as:

$$\begin{aligned} \boldsymbol{M}(\Phi_1,\Phi_2,\theta) &= \begin{bmatrix} \cos\theta & -\sin\theta \\ \sin\theta & \cos\theta \end{bmatrix} \begin{bmatrix} e^{i\Phi_1} & 0 \\ 0 & e^{i\Phi_2} \end{bmatrix} \begin{bmatrix} \cos\theta & \sin\theta \\ -\sin\theta & \cos\theta \end{bmatrix} \\ &= \begin{bmatrix} e^{i\Phi_1}\cos^2\theta + e^{i\Phi_2}\sin^2\theta & \left(e^{i\Phi_1} - e^{i\Phi_2}\right)\cos\theta\sin\theta \\ \left(e^{i\Phi_1} - e^{i\Phi_2}\right)\cos\theta\sin\theta & e^{i\Phi_1}\sin^2\theta + e^{i\Phi_2}\cos^2\theta \end{bmatrix}. \end{aligned} \tag{S13}$$

For $\theta = \frac{\pi}{4}$, Eq. S13 simplifies to:

$$\boldsymbol{M}\left(\Phi_1,\Phi_2,\frac{\pi}{4}\right) = \frac{1}{2}\begin{pmatrix} e^{i\Phi_1} + e^{i\Phi_2} & e^{i\Phi_1} - e^{i\Phi_2} \\ e^{i\Phi_1} - e^{i\Phi_2} & e^{i\Phi_1} + e^{i\Phi_2} \end{pmatrix}. \tag{S14}$$

Hence, the values of Φ_1 and Φ_2 can be obtained from:

$$\begin{cases} e^{i\Phi_1} = \boldsymbol{M}_p(\xi,\eta) + \boldsymbol{M}_s(\xi,\eta) \\ e^{i\Phi_2} = \boldsymbol{M}_p(\xi,\eta) - \boldsymbol{M}_s(\xi,\eta) \end{cases}. \tag{S15}$$

Finally, the nanopillar in-plane dimensions $L_1(\xi,\eta)$, $L_2(\xi,\eta)$ for each metasurface pixel are calculated using the *FOM* minimization procedure described in the Material and Methods section.

S3. Design of spectral phases for polarization shaping:

To generate the time-varying polarization-swept pulses (Fig. 2A), the spectral phases φ_1 and φ_2 are designed to take the following form:

$$\begin{cases} \varphi_1(\omega_J) = \frac{b_{\mathrm{II}}}{2}(\omega_J - \omega_c)^2 + b_{\mathrm{I}}(\omega_J - \omega_c) \\ \varphi_2(\omega_J) = \frac{b_{\mathrm{II}}}{2}(\omega_J - \omega_c)^2 - b_{\mathrm{I}}(\omega_J - \omega_c) \end{cases}, \tag{S16}$$

where b_{I} and b_{II} are the group delay and group delay dispersion, respectively. Here, we only focus on the time-varying polarization shaping, thus ignore the spatial part of the masking function. Substituting Eq. S16 into Eq. S15 and comparing with Eqs. S11 and S12 yields:

$$\vec{\boldsymbol{E}}_{\mathrm{out}}(t) = \sum_{J=1}^{Q} a_J e^{-i\omega_J t} e^{i\frac{b_{\mathrm{II}}}{2}(\omega_J-\omega_c)^2} \begin{bmatrix} \cos\left(b_{\mathrm{I}}(\omega_J - \omega_c)\right) \\ i\sin\left(b_{\mathrm{I}}(\omega_J - \omega_c)\right) \end{bmatrix}. \tag{S17}$$

A quarter-wave plate (QWP) with its fast axis aligned along the *x*-direction ($\vartheta = 0\pi$), placed after the shaper (Fig. 3), transforms the polarization state into:

$$\vec{\boldsymbol{E}}_{\mathrm{out}}^{\mathrm{QWP}}(t) = \sum_{J=1}^{Q} a_J e^{-i\omega_J t} e^{i\frac{b_{\mathrm{II}}}{2}(\omega_J-\omega_c)^2} \begin{bmatrix} \cos\left(b_{\mathrm{I}}(\omega_J - \omega_c)\right) \\ -\sin\left(b_{\mathrm{I}}(\omega_J - \omega_c)\right) \end{bmatrix}. \tag{S18}$$

where the corresponding $\vec{\boldsymbol{E}}_{\mathrm{out}}(t)$ and $\vec{\boldsymbol{E}}_{\mathrm{out}}^{\mathrm{QWP}}(t)$ are shown in Fig. S7.

In addition to the two representative cases with and without the QWP shown in Fig. S7, the overall pulse envelope, plotted as a curve on the surface of the Poincaré sphere for $\vec{\boldsymbol{E}}_{\mathrm{out}}^{\mathrm{QWP}}(t)$ can be readily reoriented by simply rotating the fast axis of the QWP with respect to the *x*-axis by an angle ϑ (Fig. S8).

S4. Effect of the superpixel boundaries

To examine the effect of the superpixel boundaries on the synthesis of OAM beams, we consider three superpixels (Fig. S9A), centered at $\lambda_{J=101} = \lambda_c = 800$ nm, within the metasurface. Again, we first analyze the *p*-polarization; the corresponding spatial masking function term in Eq. S6 can be expressed as:

$$\mathbf{\Gamma}_J^p(\xi - \xi_J, \eta) = \begin{cases} e^{i\,\ell \tan^{-1}\frac{\eta}{\xi - \xi_J}}, & 100 \le J \le 102, \\ 0, & \text{else} \end{cases} \tag{S19}$$

where $\ell = -1$. The output electric field resulting from superpixel at $J = 101$ is simulated by only considering spectral lines incident on that superpixel. Five representative input cw beams (wavelengths λ_j varying from 799.50 nm to 800.50 nm in 0.25 nm steps) are depicted, including two (positions a and e) at the boundaries between superpixels, two (positions b and d) at off-center positions and one (position c) at the center of the superpixel at $J = 101$ (Fig. S9B). Their electric fields are assumed to have a Gaussian input spatial distribution:

$$E_{-,j}(\xi, \eta) = u_j(\xi - \xi_j) u_j(\eta)\,, \tag{S20}$$

with $w_j \approx 25$ μm. The spatial distribution $\boldsymbol{E}_j^p(u, v, z)$ of the beam at a uv-plane after the metasurface superpixel (before the second parabolic mirror) can be calculated under Fresnel approximation as:

$$\boldsymbol{E}_j^p(u, v, z) = \frac{e^{i\frac{2\pi z}{\lambda_j}}}{i\lambda_j z} e^{\frac{i\pi}{\lambda_j z}(u^2 + v^2)} \iint_{-\infty}^{\infty} E_{-,j}(\xi, \eta) \boldsymbol{M}_p(\xi, \eta) e^{\frac{i\pi}{\lambda_j z}(\xi^2 + \eta^2)} e^{-\frac{i2\pi}{\lambda_j z}(u\xi + v\eta)} d\xi d\eta. \tag{S21}$$

The calculated intensity and phase distributions of $\boldsymbol{E}_j^p(u, v, z)$, at a representative distance of $z = (1250 \cdot \lambda_c) = 1$ mm after the metasurface, are shown in Figs. S9C and S9D, respectively. These results are experimentally confirmed by directly measuring the transmission intensity, at $z = 1$ mm after the metasurface, upon illumination of the superpixel at $J = 101$ at five spatially shifted locations using a Gaussian cw laser beam at the wavelength of λ_c and a nominal waist of ≈25 μm (Fig. S9E).

Next, we numerically simulate the experimental scenario by placing the three superpixels (Fig. S10A) at the Fourier plane of the pulse shaper and calculating the far-field electric-field distribution. The summation of all the spectral lines incident on the superpixel S_J, given by $\sum_{\lambda_J - \frac{\Delta\lambda_J}{2} \le \lambda_j < \lambda_J + \frac{\Delta\lambda_J}{2}} u_j(\xi - \xi_j) u_j(\eta) a_j e^{-i\omega_j t}$ in Eq. S8, is represented by an effective input beam at λ_J (Fig. S10B). The resulting output intensity and phase distribution of $\boldsymbol{E}_{\text{out},101}^p(x, y, t = 0)$ at $\lambda_J = 800$ nm, along with equivalent calculations performed for superpixels $J = 2$ (at $\lambda_J = 701$ nm) and $J = 200$ (at $\lambda_J = 899$ nm) are shown in Figs. S8C and S8D, respectively. The collective $\bar{I}_{\text{out}}^p$ from all the 201 superpixels, shown in Fig. 4D, closely matches the experimentally measured $\bar{I}_{\text{out}}^{p(s)}(x, y)$ (Fig. 4A, insets).

We further examine the impact of approximation in Eq. S8, where the effective input beam is approximated by $a_J\Pi(\xi-\xi_J)\cdot u_J(\eta)e^{-i\omega_J t}$ (Fig. S10E). The resulting $\bar{I}^{p}_{\mathrm{out},J}$ (Fig. S10F) and $\Psi^{p}_{\mathrm{out},J}$ (Fig. S10G) corresponding to the same three superpixels show a similar intensity null and phase singularity at the beam center as Figs. S10C and S10D, respectively, confirming that the approximation is valid.

These simulations illustrate that the deviation of the far-field intensity profile $\bar{I}^{p(s)}_{\mathrm{out}}$ from an ideal circularly symmetric Laguerre-Gaussian mode originates from spectral lines illuminating the boundaries between adjacent superpixels, introducing vertical fringes in $\bar{I}^{p(s)}_{\mathrm{out}}$ (Fig. S10C). We perform a set of far-field numerical simulations with varying superpixel widths and an optimal width of ≈115 μm is identified as a compromise between minimizing boundary effects while maintaining high spectral resolution.

S5. Extended control of spatiotemporal properties of ultrafast pulses

Similar to how an ultrafast pulse train can be decomposed into a series of frequency components, each with a corresponding amplitude and phase, any static spatial mode profile can also be decomposed into appropriately weighted spatial modes from a complete modal basis. Hence, by coherently superimposing multiple frequencies spatially, where each frequency is carrying a different spatial mode, a dynamic spatiotemporal wave packet can be realized (*25, 26*). We leverage this capability using the superpixel approach to demonstrate independent and parallel control over the spatial and temporal properties of the frequencies constituting an ultrafast pulse train, allowing arbitrary synthesis of spatiotemporal wave packets. One set of azimuthal spatial modes that form a complete and orthogonal basis is a vortex beam carrying integer topological orders. As an illustrative example, here, we demonstrate extended spatiotemporal control of femtosecond pulses by assigning five different OAM orders, one each to a preassigned set of superpixels. Two categories of spatiotemporal wave packets are realized, as discussed below.

Spatiotemporal intensity control: light-coil

A light coil, as shown in Fig. 5B, represents a spatiotemporal intensity distribution that revolves around a central axis (*26*). Along the revolving trajectory, at each azimuthal angle, the light beam remains a transform-limited ultrafast pulse, but this pulse arrives at a later time for increasing azimuthal angles, forming a helical intensity distribution.

First, we consider the coherent superposition of the constituent frequencies, sampled by *Q* superpixels, after passing through the pulse shaper. Here, we only consider the *s*-polarized output component and take advantage of the minimal unmodulated light in this polarization. To simplify the analysis without losing its generality, here, we ignore the boundary effects discussed in section S1 and S2, and assume that the superpixels impart ideal OAM modes to the constituent frequency lines. Rewriting Eqs. S11 and S12 into:

$$\begin{aligned}\boldsymbol{E}^{s}_{\mathrm{out}}(x,y,t) &= \sum_{J=1}^{Q} a_J \boldsymbol{\Upsilon}^{s}_{J}(\omega_J) e^{-i\omega_J t} \mathcal{F}^{-1}\{\boldsymbol{\Gamma}^{s}_{J}(\xi,\eta) u_J(\xi) u_J(\eta)\} \\ &= \sum_{J=1}^{Q} a_J \boldsymbol{\Upsilon}^{s}_{J}(\omega_J) e^{-i\omega_J t} \mathcal{F}^{-1}\left\{ e^{i\,\ell_J \tan^{-1}\frac{\eta}{\xi}} e^{-\frac{\xi^2+\eta^2}{w_J^2}} \right\}.\end{aligned} \tag{S22}$$

Converting Eq. S22 from the Cartesian coordinate to the polar coordinate system and expressing the analytical solution of the 2D Fourier transform in the polar coordinate (*30*):

$$\boldsymbol{E}^{s}_{\mathrm{out}}(\rho,\Omega,t) = \sum_{J=1}^{Q} a_J \boldsymbol{\Upsilon}^{s}_{J}(\omega_J) e^{-i\omega_J t} 2\pi\, i^{\ell_J} e^{i\ell_J \Omega} \boldsymbol{H}_{\ell_J}(\rho), \tag{S23}$$

where $\Omega = \tan^{-1}\frac{y}{x}$, $\boldsymbol{H}_{\ell_J}(\rho) = \int_0^\infty r e^{-\frac{r^2}{w_J^2}} \boldsymbol{B}_{\ell_J}(2\pi\rho r) dr$ is the ℓ_J-th order Hankel transform with $\boldsymbol{B}_{\ell_J}$ being the ℓ_J-th order Bessel function of the first kind, $r = \sqrt{\xi^2+\eta^2}$, and $\rho = \sqrt{x^2+y^2}$.

To achieve the light-coil in Fig. 5B, we design $\boldsymbol{\Upsilon}^{s}_{J}(\omega_J) = 1$ and $\ell_J = \begin{cases} 2 - \left\lfloor \frac{J-1}{40} \right\rfloor, & 1 \le J \le 200 \\ -2, & J = 201 \end{cases}$. The floor function in ℓ_J indicates that the 201 superpixels are divided into five groups: each group of frequencies acquires a designed vortex spatial phase front upon exiting the pulse shaper. The effective central frequencies ν_{eff} for the five groups are 416.4 THz, 394.5 THz, 374.7 THz, 356.9 THz, and 340.7 THz, corresponding to groups carrying a topological order ℓ of +2, +1, 0, –1, and –2, respectively. At a given time t, all the frequencies coherently interfere in space, leading to an azimuthally localized wave packet, with its azimuthal location determined by the phase relationship among constituting OAM orders (*40*). Because different OAM orders are carried by different groups of frequencies, this phase relationship varies as a function of time, producing a spatiotemporal light-coil. The effective revolving period can be estimated by considering that the effective time-varying phase relationship $2\pi|\Delta\nu_{\mathrm{eff}}|t$ goes through $2\pi|\Delta\ell|$ within one period, which gives an effective period of $|\Delta\ell/\Delta\nu_{\mathrm{eff}}|$, where the sign of $\Delta\ell/\Delta\nu_{\mathrm{eff}}$ determines the revolving direction. Here, $\Delta\ell = 1$ for all neighboring groups, but ν_{eff} has a non-constant spacing. The generated light-coil thus may have time-variant speed (*25*). We estimate an average revolving period of ≈ 53 fs, which agrees well with the numerical simulation result shown in Fig. 5B.

The shaped light-coil is then characterized by performing spatial interference with a tilted reference Gaussian pulse at different time delay τ:

$$\begin{aligned} I_{\mathrm{intf}}(\rho,\Omega,\tau) \\ = \left(\boldsymbol{E}^{s}_{\mathrm{out}}(\rho,\Omega,t) + \boldsymbol{E}_{\mathrm{ref}}(\rho,\Omega,t+\tau)\right)\left(\boldsymbol{E}^{s}_{\mathrm{out}}(\rho,\Omega,t) + \boldsymbol{E}_{\mathrm{ref}}(\rho,\Omega,t+\tau)\right)^{*}, \end{aligned} \tag{S24}$$

where $\boldsymbol{E}_{\mathrm{ref}}(\rho,\Omega,t+\tau) = a_{\mathrm{ref}}(\rho) e^{-i\omega_c(t+\tau)+ik_x x}$ with $a_{\mathrm{ref}}(\rho) = e^{-\frac{\rho^2}{w_{\mathrm{ref}}^2}}$, w_{ref} and k_x are the waist and wave-vector of the tilted reference beam, respectively, and $x = \rho\cos\Omega$. The interferogram from Eq. S24 contains a cross term that exhibits vertical parallel fringes coming

from the $e^{-ik_x x}$ term and the fringe contrast is modulated by the revolving electric field amplitude represented in $\boldsymbol{E}^{s}_{\mathrm{out}}$ (numerical simulations in Supplementary Movie S1).To experimentally verify the azimuthally revolving intensity profile of the shaped pulse, we reconstruct its time-dependent intensity $I_{\mathrm{meas}}(x_1, y_1, \tau)$ by calculating a moving contrast from the interferograms recorded at each time delay τ. This contrast is defined by the difference between the maximum and minimum intensity of a 10 × 10 pixel region (determined by the interference fringe spacing) centered at a spatial location (x_1, y_1). The contrast extraction is repeated for all $(x_1 + 2n_x, y_1 + 2n_y)$ coordinates, with $n_x = 1, 2, \ldots 291$ and $n_y = 1, 2, \ldots 236$, to generate $I_{\mathrm{meas}}(x, y, \tau)$. The resulted $I_{\mathrm{meas}}(x, y, \tau)$ clearly shows a revolving peak intensity as a function of time and is consistent with the numerical simulations.

Spatiotemporal phase front control: time-varying OAM

A light beam carries a time-varying OAM can be achieve by designing $\boldsymbol{\Upsilon}^{s}_{J}(\omega_J) = e^{i\frac{b_{\mathrm{II}}}{2}(\omega_J - \omega_c)^2}$ while keep the same $\ell_J = \begin{cases} 2 - \left\lfloor \frac{J-1}{40} \right\rfloor, & 1 \le J \le 200 \\ -2, & J = 201 \end{cases}$. Here, the spectral phase term $\boldsymbol{\Upsilon}^{s}_{J}(\omega_J)$ provides a chirp to the pulse. Groups of frequency comb lines carrying different OAM orders are thus engineered to arrive at different time delays, forming a spatiotemporal pulse carrying time-varying OAM (Fig. 5C).

Experimentally, we insert a 5 mm thick plate of glass after the pulse shaper, providing $b_{\mathrm{II}} = 180$ fs^2/rad, to positively chirp the pulse. Both numerical simulations and experimental results show vortex spatial structures varying from a topological order of –1 to 0 (Gaussian) then to +1 as time varies from –26 fs to +46 fs within the spatiotemporally shaped pulse (Supplementary Movie S2).

S6. Instantaneous Stokes parameters

The time-varying electric field for *p*- and *s*- polarized components can be expressed in terms of amplitude and phase as a function of time:

$$\begin{cases} \boldsymbol{E}_p(t) = A_p(t) e^{i\Psi_p(t)} \\ \boldsymbol{E}_s(t) = A_s(t) e^{i\Psi_s(t)} \end{cases}. \tag{S25}$$

At each time instant *t*, the normalized instantaneous Stokes parameters are then calculated using the following equations:

$$\begin{cases} I(t) = A_p^2(t) + A_s^2(t) \\ Q(t) = \left(A_p^2(t) - A_s^2(t)\right)/I(t) \\ U(t) = 2A_p(t)A_s(t)\cos\left(\Delta\Psi(t)\right)/I(t) \\ V(t) = 2A_p(t)A_s(t)\sin\left(\Delta\Psi(t)\right)/I(t) \end{cases}, \tag{S26}$$

where $\Delta\Psi(t) = \Psi_s(t) - \Psi_p(t)$ is the relative phase between *s*- and *p*-polarized components.

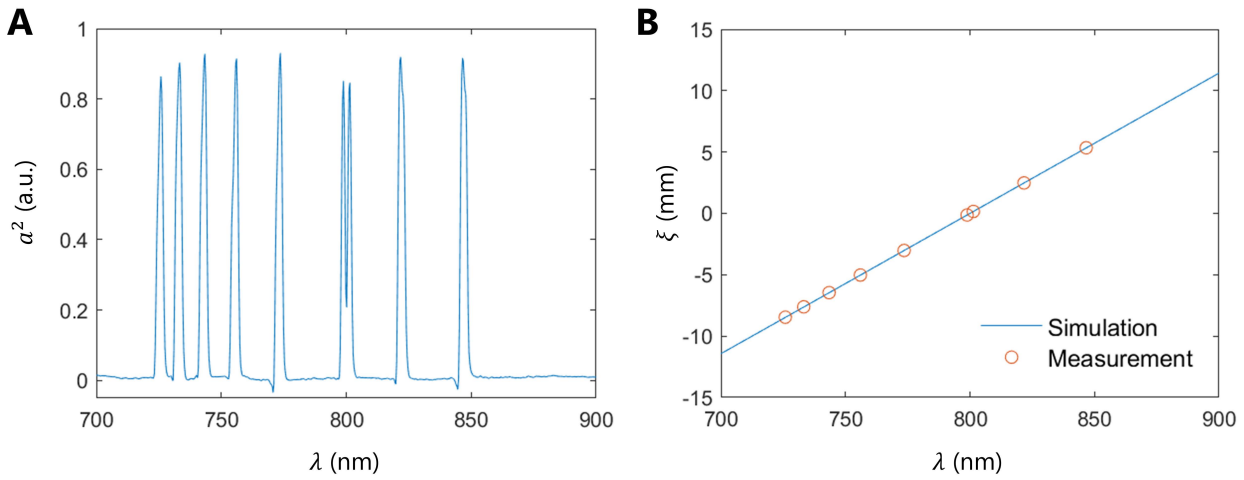

Fig. S1. Spatial dispersion of λ *vs.* ξ. (A) Normalized spectrum of an input pulse transmitted through a reference mask containing nine half-wave plate metasurface superpixels used for spectral calibration, and alignment of the metasurface at the Fourier plane. **(B)** The calibrated quasi-linear relationship between ξ and λ at the Fourier plane. The red circles correspond to the peaks in (A) and the blue line is calculated using $\xi_j = (\lambda_j - \lambda_c) f/\Lambda_G$, where f = 381 mm is the focal length of the parabolic mirror and $\Lambda_G = (1/300)$ mm is the grating pitch.

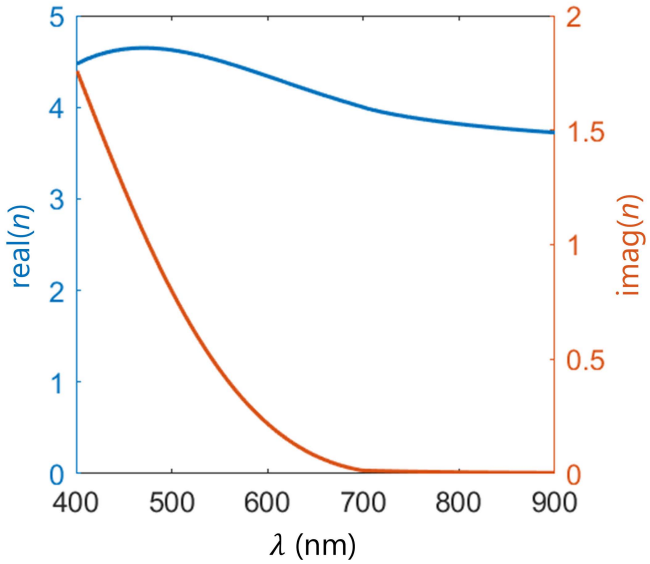

Fig. S2. Refractive index of a-Si. The real and imaginary part of the refractive index n *vs.* λ, for a-Si, measured using spectroscopic ellipsometry. The a-Si film is deposited on an oxide coated reference Si substrate (thermal oxide thickness = 300 nm) using PECVD.

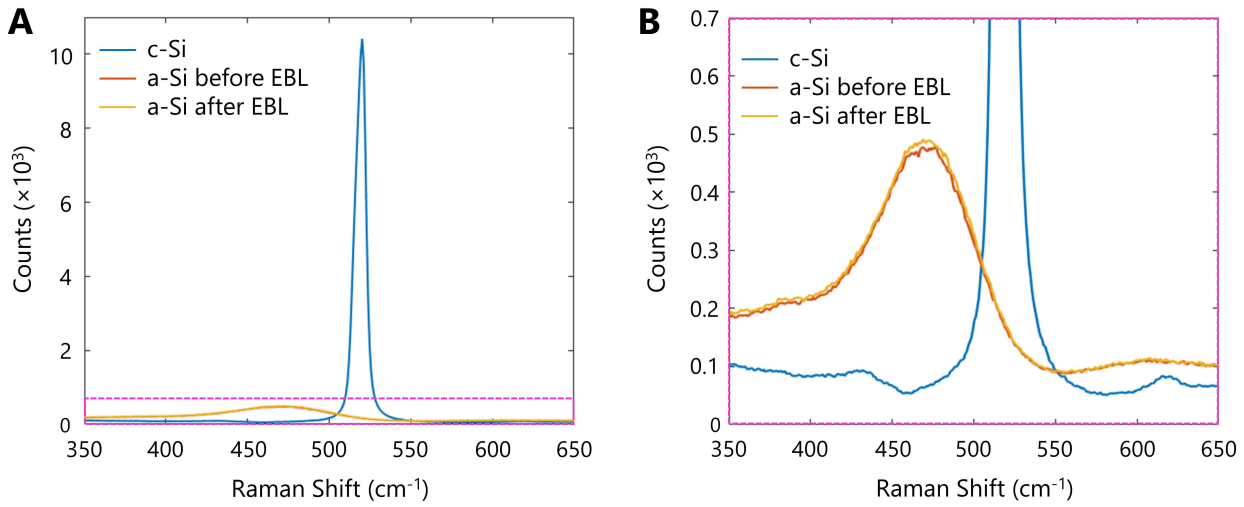

Fig. S3. Raman spectra of a-Si before and after exposure to electron beam. (**A**) The Raman spectra from a polished crystalline Si (c-Si) wafer (blue), PECVD deposited 650 nm thick a-Si film on a fused-silica substrate before (orange) and after (yellow) exposure to 100 keV electron beam. (**B**) Zoom-in plot of the Raman spectra corresponding to the pink dashed box in (A). The measurements are performed at room temperature using an excitation wavelength of 532 nm (incident power: ≈3 mW) focused onto the sample with a 50× objective (numerical aperture = 0.35, FWHM spot size: 760 nm). The measured spectra show no observable change between the a-Si samples before and after electron-beam exposure, indicating that any morphological change of the a-Si film after exposure is minimal, and the film remains amorphous.

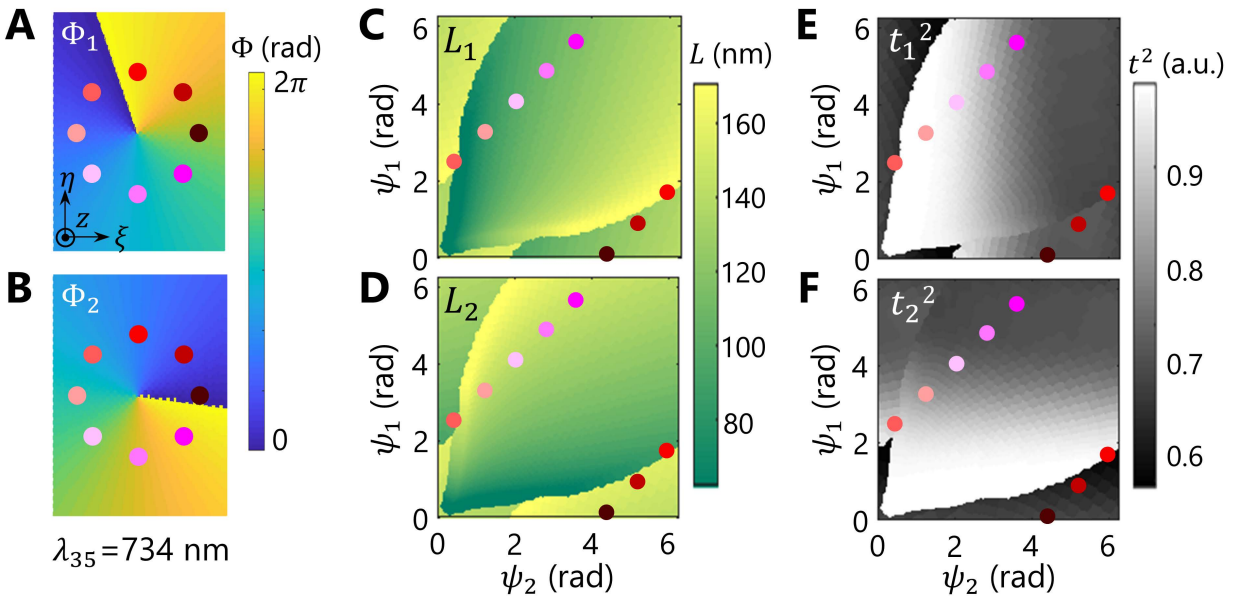

Fig. S4. Representative nanopillar library to achieve the targeted masking function. (**A** and **B**) Targeted phase topographies Φ_1 and Φ_2, at $\lambda_{35} = 734$ nm, to achieve the masking function in Fig. 2. (**C** and **D**) Simulated nanopillar in-plane dimensions L_1 and L_2 that can deliver any combination of ψ_1 and ψ_2 covering the full $[0,\ 2\pi]$ range along the two birefringent axes. (**E** and **F**) Simulated transmission coefficients corresponding to the choice of L_1 and L_2 shown in (C) and (D). The colored dots in (C) to (F) correspond to the designs for eight representative targeted (Φ_1, Φ_2) combinations in (A) and (B).

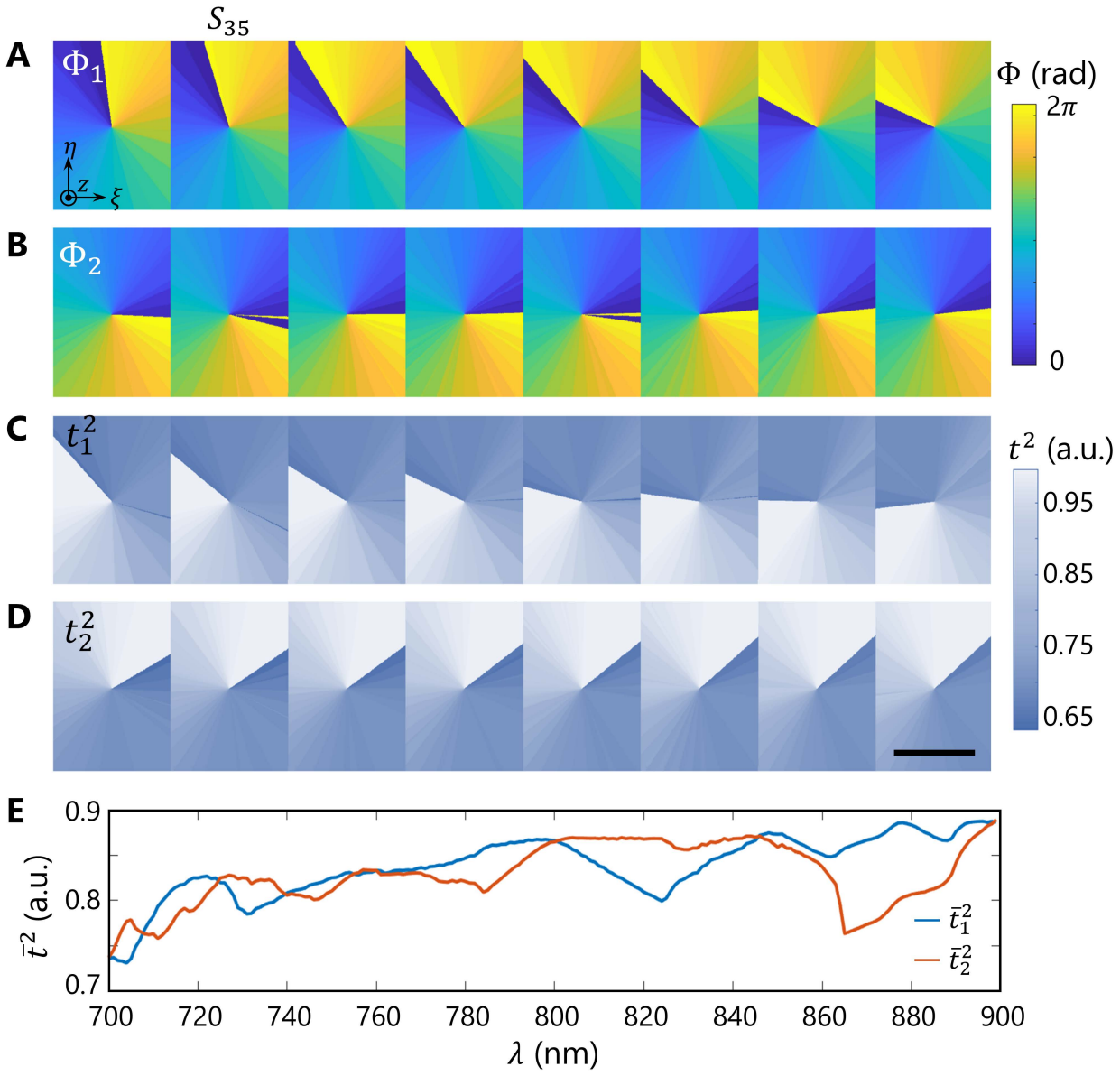

Fig. S5. Simulated phase and intensity transmission maps for the eight representative superpixels shown in Fig. 2. (**A** and **B**) the simulated phase maps to achieve the Φ_1 and Φ_2 designs shown in Fig. 2D. (**C** and **D**) The simulated transmission maps t_1^2 and t_2^2 for the corresponding superpixels in (A) and (B). Scale bar: 100 μm. (**E**) The average $\bar{t}_1^2$ and $\bar{t}_2^2$ for each superpixel S_J.

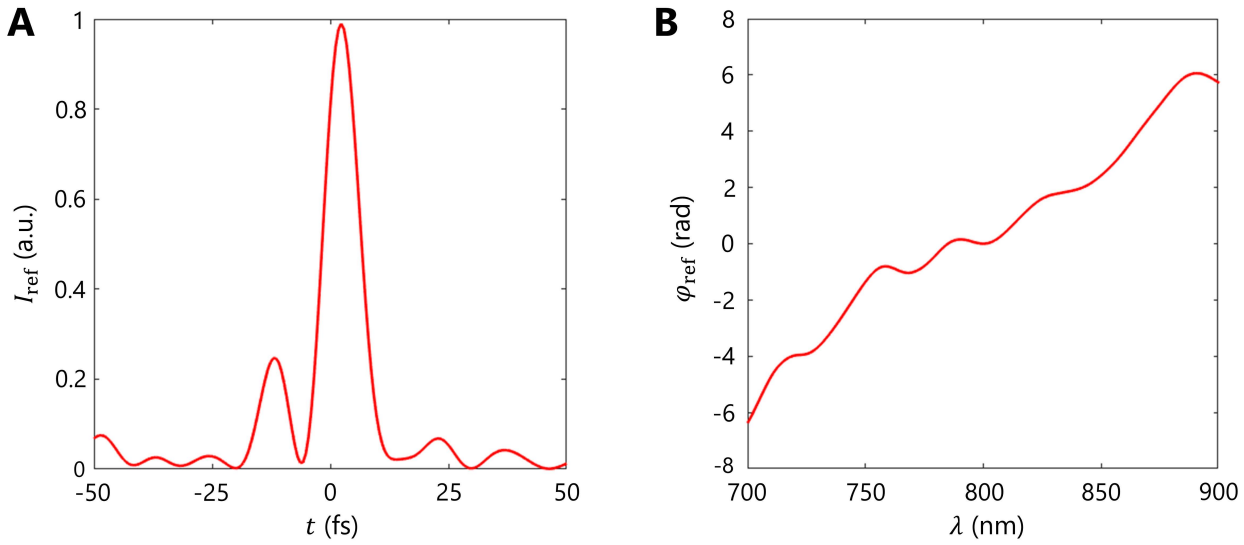

Fig. S6. SPIDER measurement of the reference pulse. (A-B) The temporal intensity (A) and spectral phase (B) of the reference pulse measured using the SPIDER setup.

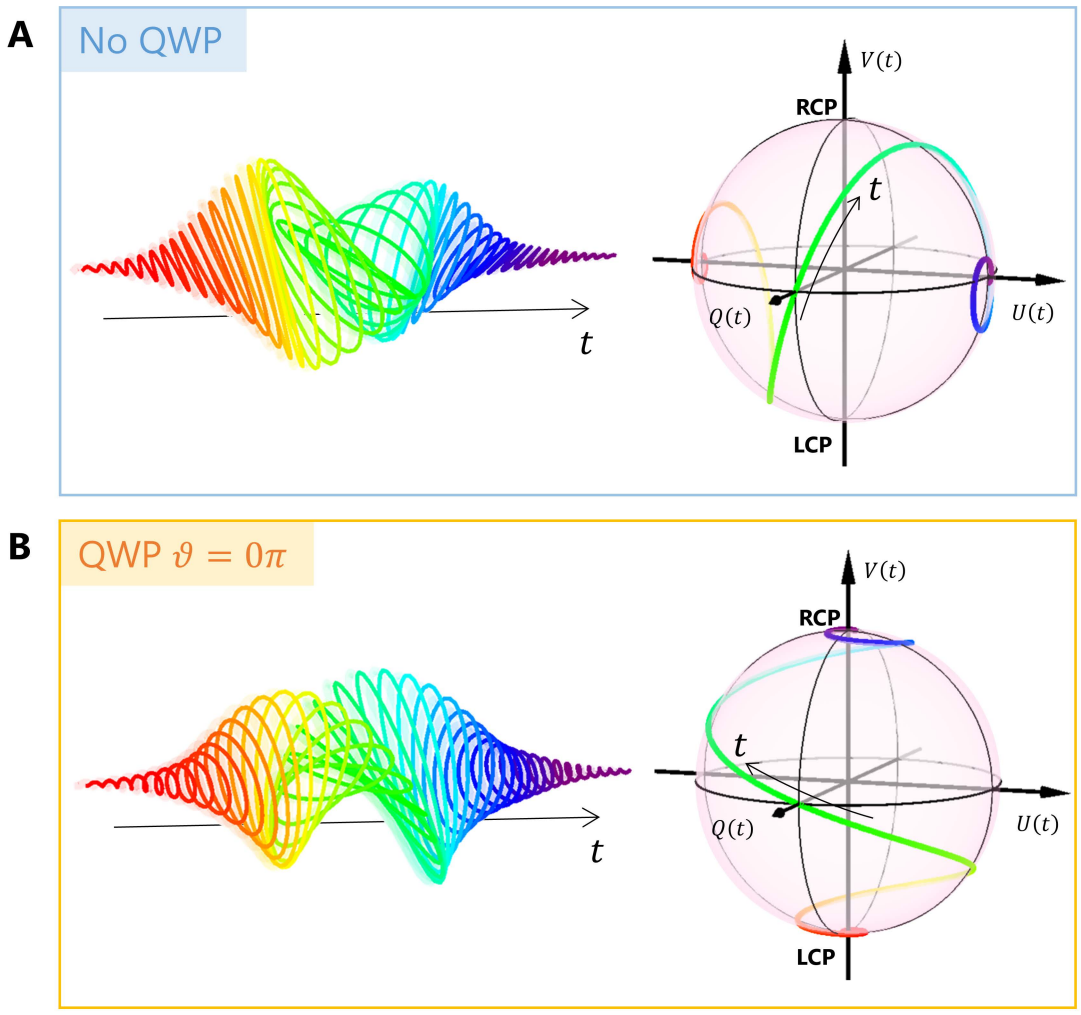

Fig. S7. Time-varying polarization control. Simulated electric-field waveforms and corresponding time-varying polarization states (section S4) with $b_{\mathrm{II}} = 100$ fs^2/rad and $b_{\mathrm{I}}/b_{\mathrm{II}} = 0.1$ rad/fs. (**A**) With no QWP at the output of the pulse shaper, the polarization state of $\vec{\boldsymbol{E}}_{\mathrm{out}}(t)$, denoted by a curve on the Poincaré sphere, varies adiabatically from $-45°$ linear → elliptical → horizontal linear → elliptical → $+45°$ linear. (**B**) When a QWP, with its fast axis aligned parallel to the *x*-direction ($\vartheta = 0\pi$), is added after the pulse shaper, the corresponding polarization state of $\vec{\boldsymbol{E}}_{\mathrm{out}}^{\mathrm{QWP}}(t)$ varies from left circular → elliptical → horizontal linear → elliptical → right circular. $Q(t)$, $U(t)$, $V(t)$ are the corresponding Stokes parameters (defined in Supplementary Text, S5).

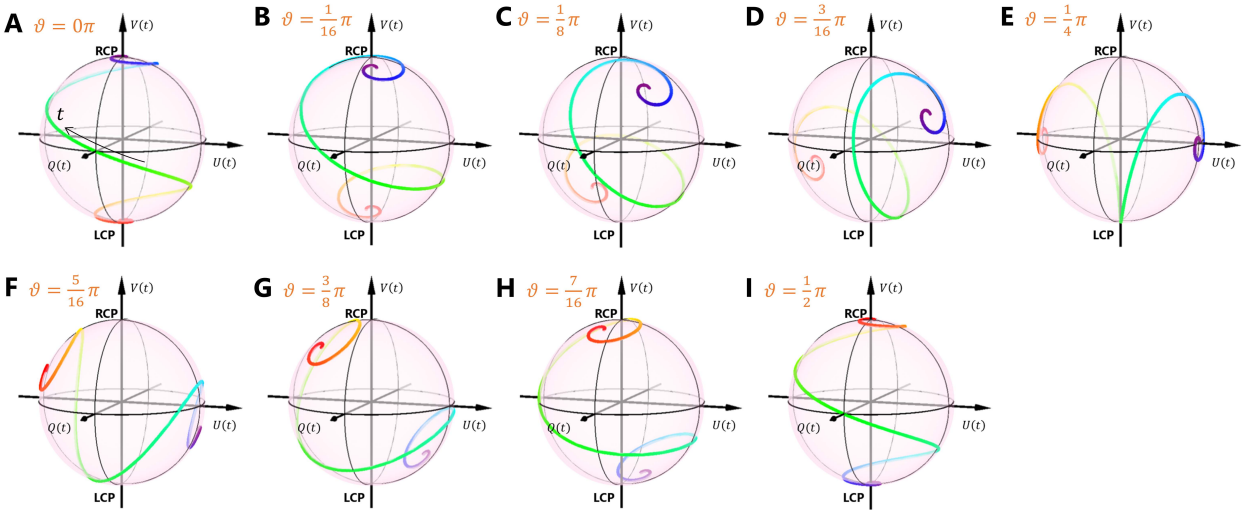

Fig. S8. Ready time-varying polarization control using a QWP. (**A-I**) The instantaneous polarization states of simulated $\vec{E}_{\mathrm{out}}^{\mathrm{QWP}}(t)$ plotted on the surface of the Poincaré sphere as the fast-axis of the QWP at the output of the pulse shaper is rotated from $\vartheta = 0\pi$ to $\vartheta = \pi/2$ with respect to the *x*-direction.

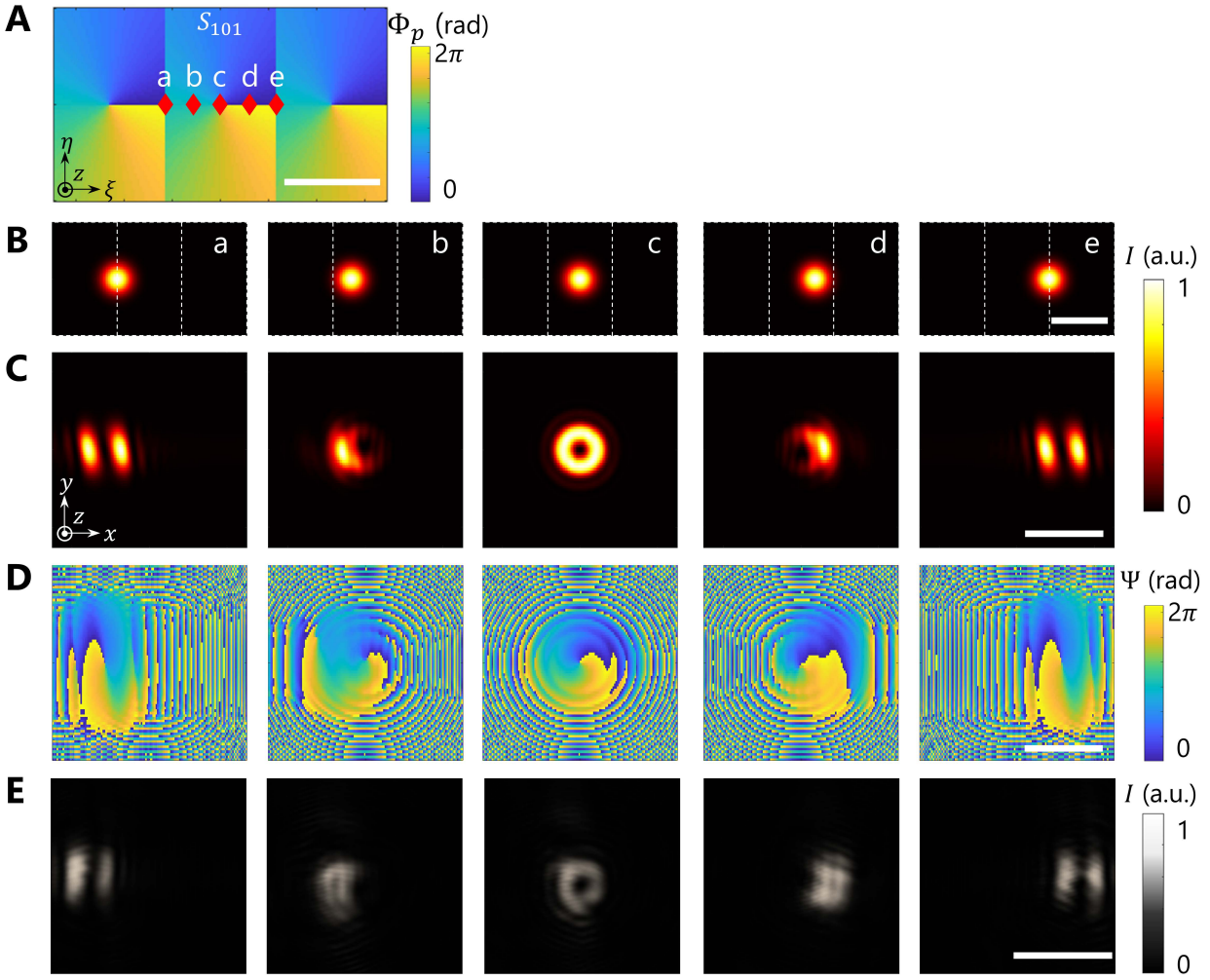

Fig. S9. Superpixel boundary effect on the Fresnel far-field intensity distribution from a superpixel designed to impart a topological charge of –1. (**A**) $\Phi_J^p(\xi,\eta)$ for three adjacent superpixels S_{J-1}, S_J, and S_{J+1} for $J = 101$, centered at λ_c, each designed to impart a 2D spiral phase with $\ell_J = -1$ to the corresponding ω_J. Red trapezoids: five representative spatially shifted excitation positions (marked a-e). (**B**) Superpixel at $J = 101$ illuminated at the corresponding spatial locations marked a-e in (A). Dotted white lines indicate the boundary between adjacent superpixels. The excitation beam waist is ≈25 μm. Numerically simulated far-field intensity (**C**) and phase (**D**) distributions, at $z = 1$ mm, upon transmission through the metasurface superpixel (each panel corresponds to the excitation condition in (B)). (**E**) Experimentally measured transmitted intensity distribution, at $z = 1$ mm, upon illumination of the superpixel at $J = 101$ with a cw-laser at 800 nm at the nominal locations indicated in (B). Scale bars: 100 μm.

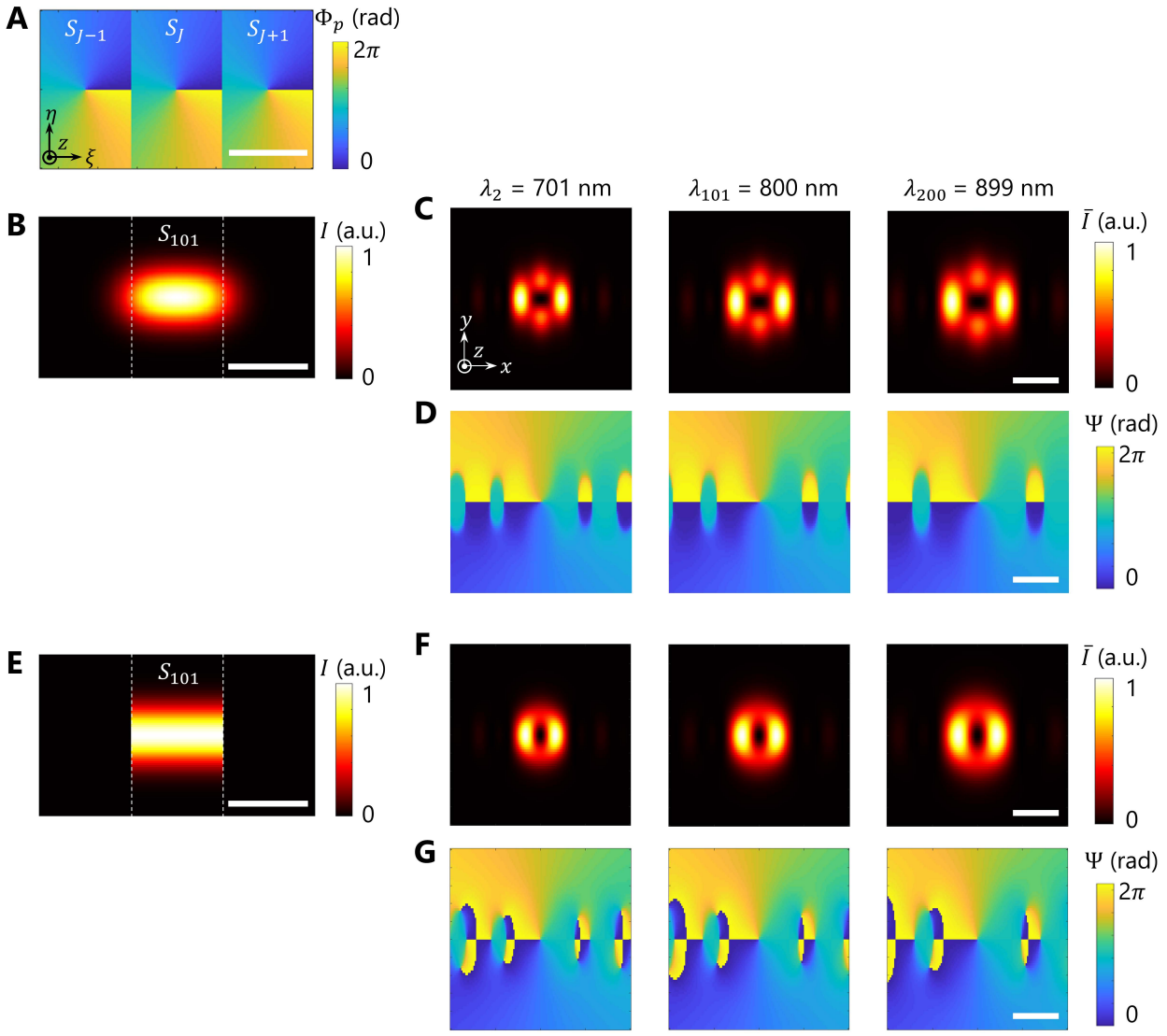

Fig. S10. Superpixel boundary effect on the spatial term of the shaped output pulse $E^p_{\mathrm{out},J}(x,y)$ from a superpixel designed to impart a topological charge of –1. (**A**) Representative $\Phi^p_J(\xi,\eta)$ for three adjacent superpixels S_{J-1}, S_J, and S_{J+1}. Scale bar: 100 μm. (**B**) The effective incident intensity distribution illuminating the superpixel $J = 101$ at $\lambda_J = 800$ nm. Scale bar: 100 μm. Calculated $\bar{I}^p_{\mathrm{out},J}$ (**C**) and $\Psi^p_{\mathrm{out},J}$ (**D**) for superpixels $J = 2$ (at $\lambda_J = 701$ nm), $J = 101$ (at $\lambda_J = 800$ nm), and $J = 200$ (at $\lambda_J = 899$ nm). Scale bars: 5 mm. (**E**) The approximated incident intensity distribution following Eq. S8 (scale bar: 100 μm), along with the corresponding $\bar{I}^p_{\mathrm{out},J}$ (**F**) and $\Psi^p_{\mathrm{out},J}$ (**G**) (scale bars: 5 mm).

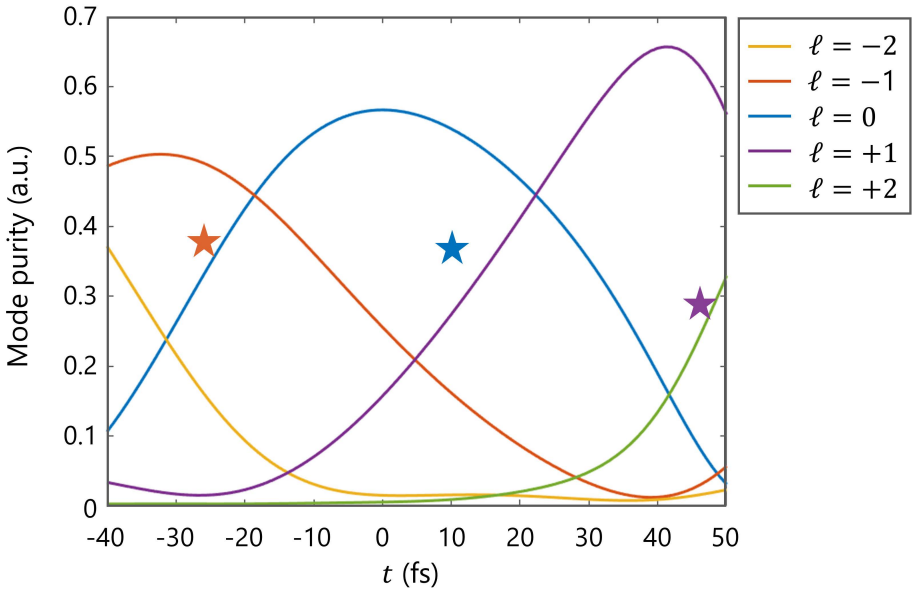

Fig. S11. Mode-purity of the time-varying OAM pulse. Colored lines represent the retrieved mode-purity of OAM orders $\ell = -2$ (yellow), -1 (orange), 0 (blue), $+1$ (purple), $+2$ (green), respectively for the simulated time varying OAM pulse shown in Fig. 5C. Colored stars denote the retrieved mode-purity of the three experimental snapshots (Fig. 5C, Inset) for OAM orders $\ell = -1$ (orange), 0 (blue), $+1$ (purple), respectively.

Movie S1. Spatiotemporal intensity control: light-coil. An ultrafast pulse engineered to encode a time-varying spatial intensity distribution that revolves around a central axis. Numerically simulated $\Psi_{\mathrm{sim}}(x, y, t)$ (top left) and $I_{\mathrm{sim}}(x, y, t)$ (top right) of the designed light-coil exhibiting an azimuthally revolving intensity I_{sim}, within which the spatial phase front Ψ_{sim} remains flat. Experimentally measured interferogram $I_{\mathrm{intf}}(x, y, \tau)$ (bottom left), acquired by interfering $\boldsymbol{E}_{\mathrm{out}}$ with a reference $\boldsymbol{E}_{\mathrm{in}}$, shows parallel fringes with a revolving fringe contrast, confirming a flat phase front in the synthesized pulse. The reconstructed $I_{\mathrm{meas}}(x, y, \tau)$, shown in the bottom right, closely matches $I_{\mathrm{sim}}(x, y, t)$.

Movie S2. Spatiotemporal phase control: time-varying OAM. By chirping the frequency groups carrying different OAM orders, an ultrafast pulse is engineered to carry time-varying OAM. Top: numerically simulated $\Psi_{\mathrm{sim}}(x, y, t)$ shows three different vortex phase topographies, varying from a topological order of –1 to 0 then to +1 as a function of time. Bottom: experimentally measured $I_{\mathrm{intf}}(x, y, \tau)$ changes from fringes with a down-opening fork-dislocation to parallel fringes to fringes with an up-opening dislocation, as τ increases.

REFERENCES AND NOTES

1. N. Dudovich, D. Oron, Y. Silberberg, Single-pulse coherently controlled nonlinear Raman spectroscopy and microscopy. *Nature* **418**, 512-514 (2002).

2. T. Brixner, F. J. García de Abajo, J. Schneider, W. Pfeiffer, Nanoscopic ultrafast space-time-resolved spectroscopy. *Phys. Rev. Lett.* **95**, 093901 (2005).

3. M. Aeschlimann, M. Bauer, D. Bayer, T. Brixner, S. Cunovic, F. Dimler, A. Fischer, W. Pfeiffer, M. Rohmer, C. Schneider, F. Steeb, C. Strüber, D. V. Voronine, Spatiotemporal control of nanooptical excitations. *Proc. Natl. Acad. Sci.* **107**, 5329-5333 (2010).

4. P. Hommelhoff, M. Kling, *Attosecond Nanophysics: From Basic Science to Applications*. (John Wiley & Sons, 2015).

5. National Academies of Sciences, Engineering, and Medicine, *Opportunities in Intense Ultrafast Lasers: Reaching for the Brightest Light* (The National Academies Press, Washington, DC, 2018).

6. R. Thomson, C. Leburn, D. Reid, Eds., *Ultrafast Nonlinear Optics* (Springer, 2013).

7. T. Südmeyer, S. V. Marchese, S. Hashimoto, C. R. E. Baer, G. Gingras, B. Witzel, U. Keller, Femtosecond laser oscillators for high-field science. *Nat. Photonics* **2**, 599-604 (2008).

8. A. J. Metcalf, T. Anderson, C. F. Bender, S. Blakeslee, W. Brand, D. R. Carlson, W. D. Cochran, S. A. Diddams, M. Endl, C. Fredrick, S. Halverson, D. D. Hickstein, F. Hearty, J. Jennings, S. Kanodia, K. F. Kaplan, E. Levi, E. Lubar, S. Mahadevan, A. Monson, J. P. Ninan, C. Nitroy, S. Osterman, S. B. Papp, F. Quinlan, L. Ramsey, P. Robertson, A. Roy, C. Schwab, S. Sigurdsson, K. Srinivasan, G. Stefansson, D. A. Sterner, R. Terrien, A. Wolszczan, J. T. Wright, G. Ycas, Stellar spectroscopy in the near-infrared with a laser frequency comb. *Optica* **6**, 233-239 (2019).

9. N. Picqué, T. W. Hänsch, Frequency comb spectroscopy. *Nat. Photonics* **13**, 146-157 (2019).

10. S. A. Diddams, K. Vahala, T. Udem, Optical frequency combs: Coherently uniting the electromagnetic spectrum. *Science* **369**, eaay3676 (2020).

11. J. X. Tull, M. A. Dugan, W. S. Warren, High-resolution, ultrafast laser pulse shaping and its applications. *Advances in Magnetic and Optical Resonance* **20**, 1 (1997).

12. A. M. Weiner, Ultrafast optical pulse shaping: A tutorial review. *Opt. Commun.* **284**, 3669-3692 (2011).

13. D. Strickland, G. Mourou, Compression of amplified chirped optical pulses. *Opt. Commun.* **55**, 447-449 (1985).

14. S. T. Cundiff, A. M. Weiner, Optical arbitrary waveform generation. *Nat. Photonics* **4**, 760-766 (2010).

15. M. Yessenov, L. A. Hall, K. L. Schepler, A. F. Abouraddy, Space-time wave packets, http://arxiv.org/abs/2201.08297 (2022).

16. A. H. Dorrah, F. Capasso, Tunable structured light with flat optics. *Science* **376**, eabi6860 (2022).

17. A. Korobenko, A. A. Milner, J. W. Hepburn, V. Milner, Rotational spectroscopy with an optical centrifuge. *Phys. Chem. Chem. Phys.* **16**, 4071-4076 (2014).

18. M. Padgett, R. Bowman, Tweezers with a twist. *Nat. Photonics* **5**, 343-348 (2011).

19. Y. Dai, Z. Zhou, A. Ghosh, R. S. K. Mong, A. Kubo, C.-B. Huang, H. Petek, Plasmonic topological quasiparticle on the nanometre and femtosecond scales. *Nature* **588**, 616-619 (2020).

20. J. W. McIver, D. Hsieh, H. Steinberg, P. Jarillo-Herrero, N. Gedik, Control over topological insulator photocurrents with light polarization. *Nat. Nanotechnol.* **7**, 96-100 (2012).

21. F. Kong, C. Zhang, F. Bouchard, Z. Li, G. G. Brown, D. H. Ko, T. J. Hammond, L. Arissian, R. W. Boyd, E. Karimi, P. B. Corkum, Controlling the orbital angular momentum of high harmonic vortices. *Nat. Commun.* **8**, 14970 (2017).

22. L. Rego, K. M. Dorney, N. J. Brooks, Q. L. Nguyen, C.-T. Liao, J. San Román, D. E. Couch, A. Liu, E. Pisanty, M. Lewenstein, L. Plaja, H. C. Kapteyn, M. M. Murnane, C. Hernández-García, Generation of extreme-ultraviolet beams with time-varying orbital angular momentum. *Science* **364**, eaaw9486 (2019).

23. T. Fan, P. Grychtol, R. Knut, C. Hernández-García, D. D. Hickstein, D. Zusin, C. Gentry, F. J. Dollar, C. A. Mancuso, C. W. Hogle, O. Kfir, D. Legut, K. Carva, J. L. Ellis, K. M. Dorney, C. Chen, O. G. Shpyrko, E. E. Fullerton, O. Cohen, P. M. Oppeneer, D. B. Milošević, A. Becker, A. A. Jaroń-Becker, T. Popmintchev, M. M. Murnane, H. C. Kapteyn, Bright circularly polarized soft X-ray high harmonics for X-ray magnetic circular dichroism. *Proc. Natl. Acad. Sci.* **112**, 14206-14211 (2015).

24. L. Rego, N. J. Brooks, Q. L. D. Nguyen, J. San Román, I. Binnie, L. Plaja, H. C. Kapteyn, M .M. Murnane, C. Hernández-García, Necklace-structured high-harmonic generation for low-divergence, soft x-ray harmonic combs with tunable line spacing. *Sci. Adv.* **8**, eabj7380 (2022).

25. Z. Zhao, H. Song, R. Zhang, K. Pang, C. Liu, H. Song, A. Almaiman, K. Manukyan, H. Zhou, B. Lynn, R. W. Boyd, M. Tur, A. E. Willner, Dynamic spatiotemporal beams that combine two independent and controllable orbital-angular-momenta using multiple optical-frequency-comb lines. *Nat. Commun.* **11**, 4099 (2020).

26. G. Pariente, F. Quéré, Spatio-temporal light springs: extended encoding of orbital angular momentum in ultrashort pulses. *Opt. Lett.* **40**, 2037-2040 (2015).

27. S. Fu, Y. Zhai, J. Zhang, X. Liu, R. Song, H. Zhou, C. Gao, Universal orbital angular momentum spectrum analyzer for beams. *PhotoniX* **1**, 19 (2020).

28. A. Forbes, M. de Oliveira, M. R. Dennis, Structured light. *Nat. Photonics* **15**, 253-262 (2021).

29. D. H. Froula, D. Turnbull, A. S. Davies, T. J. Kessler, D. Haberberger, J. P. Palastro, S.-W. Bahk, I. A. Begishev, R. Boni, S. Bucht, J. Katz, J. L. Shaw, Spatiotemporal control of laser intensity. *Nat. Photonics* **12**, 262-265 (2018).

30. A. Chong, C. Wan, J. Chen, Q. Zhan, Generation of spatiotemporal optical vortices with controllable transverse orbital angular momentum. *Nat. Photonics* **14**, 350-354 (2020).

31. B. E. Schmidt, P. Lassonde, G. Ernotte, M. Clerici, R. Morandotti, H. Ibrahim, F. Légaré, Decoupling frequencies, amplitudes and phases in nonlinear optics. *Sci. Rep.*, **7**, 7861 (2017).

32. J. Yang, S. Gurung, S. Bej, P. Ni, and H. W. H. Lee, Active optical metasurfaces: comprehensive review on physics, mechanisms, and prospective applications, *Rep. Prog. Phys.* **85**, 036101 (2022).

33. S. Divitt, W. Zhu, C. Zhang, H. J. Lezec, A. Agrawal, Ultrafast optical pulse shaping using dielectric metasurfaces. *Science* **364**, 890 (2019).

34. Y. Yang, W. Wang, A. Boulesbaa, I. I. Kravchenko, D. P. Briggs, A. Puretzky, D. Geohegan, J. Valentine, Nonlinear Fano-resonant dielectric metasurfaces. *Nano Lett.* **15**, 7388-7393 (2015).

35. V. Liu, S. Fan, S^4: A free electromagnetic solver for layered periodic structures. *Comput. Phys. Commun.* **183**, 2233-2244 (2012).

36. W. J. Walecki, D. N. Fittinghoff, A. L. Smirl, R. Trebino, Characterization of the polarization state of weak ultrashort coherent signals by dual-channel spectral interferometry. *Opt. Lett.* **22**, 81-83 (1997).

37. A. Monmayrant, S. Weber, B. Chatel, A newcomer's guide to ultrashort pulse shaping and characterization. *J. Phys. B: At. Mol. Opt. Phys.* **43**, 103001 (2010).

38. L. Lepetit, G. Chériaux, M. Joffre, Linear techniques of phase measurement by femtosecond spectral interferometry for applications in spectroscopy. *J. Opt. Soc. Am. B* **12**, 2467-2474 (1995).

39. M. B. Danailov, I. P. Christov, Time-space shaping of light pulses by Fourier optical processing. *J. Mod. Opt.* **36**, 725-731 (1989).

40. A. M. Yao, M. J. Padgett, Orbital angular momentum: origins, behavior and applications. *Adv. Opt. Photonics* **3**, 161-204 (2011).